

Title	Structure Analysis of Chloroplast Type Ferredoxin at 2.8Å Resolution
Author(s)	Fukuyama, Keiichi
Citation	大阪大学, 1979, 博士論文
Version Type	VoR
URL	https://hdl.handle.net/11094/27747
rights	
Note	

Osaka University Knowledge Archive : OUKA

<https://ir.library.osaka-u.ac.jp/>

Osaka University

Structure Analysis of Chloroplast Type Ferredoxin

at 2.8Å Resolution

1979

Keiichi Fukuyama

Structure Analysis of Chloroplast Type Ferredoxin
at 2.8 Å Resolution

A Doctoral Thesis
Submitted by
Keiichi Fukuyama
to
Faculty of Science
Osaka University
1979

Acknowledgements

This work was performed under supervision of Professor Masao Kakudo of the Institute for Protein Research, Osaka University. The author is greatly indebted to Professor Masao Kakudo for his continuing guidance and encouragement. He wishes to express his thanks to Professor Yukiteru Katsube for his invaluable suggestions and encouragement throughout the work. He is also express his thanks to Drs. Nobuo Tanaka and Yoshiki Matsuura at the Institute for Protein Research, Osaka University, and to Dr. Tomitake Tsukihara at Faculty of Engineering, Tottori University (staying at Purdue University from February 1978) for helpful discussions and suggestions. He is also grateful to Professor Hiroshi Matsubara and Dr. Keishiro Wada of Faculty of Science, Osaka University, for the discussion of biochemical study. Finally he wishes to thank the members of Kakudo Laboratory and Katsube Laboratory for their active participation and kind assistance in this work.

Contents

I. Introduction	1
I-1. History of ferredoxins	1
I-2. Properties and functions of ferredoxins	2
I-3. Amino acid sequences and molecular evolution	3
II. Crystal structure analysis of <i>Spirulina platensis</i> ferredoxin	10
II-1. Experimental	10
Crystallization of the protein	10
Crystal data	10
Preparation of heavy atom derivatives	11
Intensity measurement	12
Data correction	13
II-2. Phase determination	23
Location of heavy atoms and refinement of their parameters	23
Determination of absolute configuration and location of iron atoms	24
Calculation of electron density map	30
II-3. Interpretation of electron density map	37
Molecular model at low resolution	37
Model building at 2.8 Å resolution	37
II-4. Description of structure of <i>Spirulina platensis</i> ferredoxin	42
Main chain folding	42
Heavy atom binding site	42
Chelate structure of active center	43

NH...S hydrogen bond	43
III. Crystal structure analysis of <i>Aphanothece sacrum</i>	
ferredoxin at 5 Å resolution	48
III-1. Experimental	48
III-2. Intensity measurement	49
III-3. Phase determination	50
III-4. Molecular model at 5 Å resolution	51
IV. Discussion	61
IV-1. X-Ray analysis	61
IV-2. Environment of cluster	62
IV-3. Electron transfer mechanism	64
IV-4. Molecular evolution	66
IV-5. Advance in future	73
References	75
List of publications	80

I. Introduction

I-1. History of ferredoxins

The name of ferredoxin was given in 1962 by Mortenson *et al.* to the non-heme iron protein isolated from *Clostridium pasteurianum*, anaerobic bacterium (1). Ferredoxin was later found in other nonphotosynthetic anaerobic bacteria (2,3), therefore the distribution seemed likely to be limited to anaerobic bacteria which contain an active hydrogenase system. While, in 1962, Tagawa and Arnon discovered a ferredoxin-like protein from spinach; ferredoxin was able to replace the protein in the system of NADP-reduction by chloroplast (4). They also showed that the ferredoxin-like proteins are invariably present in photosynthetic cells and that the proteins play a key role in the energy transfer mechanism in photosynthesis (4,5). Since then, the name of ferredoxin was proposed to be applied to these proteins, and as well to the proteins which were called by different names such as methemoglobin reducing factor (6), TPN-reducing factor (7), PPNR (8), and heme-reducing factor (9). The name of ferredoxin is now applied to the family of the proteins which are able to catalyze the photoreduction of NADP by isolated chloroplast and contain equimolar amounts of non-heme iron atoms and labile sulfur atoms and have very low oxidation-reduction potential (about -410 mV) (5,10). Ferredoxin is one of proteins which have been studied most extensively from standpoints of biochemistry and physicalchemistry; for example, the

amino acid sequences of more than twenty species of ferredoxins have been determined at present, since the sequence of *Clostridium pasteurianum* ferredoxin was at first determined in 1964 by Tanaka *et al.* (11).

I-2. Properties and functions of ferredoxins

Ferredoxins are widely spread in nature, from bacteria to green plants, and differ in their properties according to the source of the proteins. Ferredoxins are roughly classified into two types; bacterial type and chloroplast type. The bacterial type is further subdivided to anaerobic type and photosynthetic type; the former has two 4Fe-4S* clusters in a molecule with the molecular weight of about 6,000, and the latter has one 4Fe-4S* cluster per molecule with the molecular weight of about 9,000. The chloroplast type ferredoxin has one 2Fe-2S* cluster per molecule with the molecular weight of about 11,000. The X-ray structure analysis of an anaerobic type bacterial ferredoxin was completed by Adman *et al.* in 1973, revealing that each 4Fe-4S* cluster has distorted cubic form, and that four sulfur atoms of cysteine coordinate to four iron atoms of each cluster (12). On the other hand, the chloroplast type ferredoxin has been studied only by spectroscopic method. The details of the properties and the structures of the clusters are given in Table I-1 and Figs. I-1 and I-2 for both types of ferredoxins.

The absorption spectra of chloroplast type ferredoxins are similar to each other. The spinach ferredoxin, for

example, has absorption maxima at 463, 420, and 325 nm in visible light region, and 274 nm in ultraviolet region in the oxidized state (4). The absorptions in visible light region are mainly due to the cluster consisted of iron and inorganic sulfur atoms (13,14). The two iron atoms in the oxidized state are high spin ferric, and couple antiferromagnetically to each other to give no EPR signal at low temperature (15-17). The oxidized ferredoxin is reduced by sodium dithionite to accept one electron per molecule (18). The ferredoxin in the reduced state shows $g=1.94$ in EPR spectrum below 77 K (19).

Ferredoxin plays an important role in the electron transfer mechanisms of photosynthesis (5,20); ferredoxin reduced photochemically in the system I reduces NADP through a flavoprotein named ferredoxin-NADP reductase (21). The role of ferredoxin in the system of photosynthesis is illustrated in Fig. I-3. Ferredoxin also acts as an electron carrier between hydrogenase and chloroplast (22). Ferredoxin, as stated previously, spreads not only in green plants but also in photosynthetic and anaerobic bacteria, so ferredoxin functions in such variety systems of nitrogen fixation (23), nitrite reduction (24), reduction carboxylation reaction (25), and nitrogen assimilation (26).

I-3. Amino acid sequences and molecular evolution

The chloroplast type ferredoxins are composed of 96-98 amino acid residues. They usually lack of or have a few of residues of methionine, tryptophan, histidine, and

arginine (10). The notable feature of amino acid compositions is that they contain a large amount of acidic residues, aspartic and glutamic acids. Since there is an excess of acidic over basic residues, they show acidic nature, as bacterial type ferredoxins (10). The sequences of the chloroplast type ferredoxins have been determined for sixteen species at present, and they are given in Table I-2 by one letter notation (27). They contain 5-6 cysteinyl residues per molecule, and the Cys41, Cys46, Cys49, and Cys80 are completely invariant. Therefore, the sulfur atoms of the four cysteinyl residues have been supposed to coordinate to the two iron atoms of the cluster. It has been suggested that two types ferredoxins have common ancestor from the comparison of amino acid sequences of *Clostridium butyricum* and spinach ferredoxins (28).

A phylogenetic tree of chloroplast type ferredoxins (Fig. I-4) was constructed by a matrix method (29) on the basis of the number of amino acid differences, where a deletion or insertion was counted as one difference. The tree suggests that the higher plant ferredoxin is similar to each other, while that the blue-green algal ferredoxin is remote to each other (27).

The X-ray analysis of the series of ferredoxins will yield not only the structural basis for their biochemical behaviour, but also some basic knowledge for the molecular evolution. At the present time, the determination of three-dimensional structure of chloroplast type ferredoxin is particularly noteworthy from view point already

described. Therefore, the structure determinations of two ferredoxins of chloroplast type, *Spirulina platensis* and *Aphanothece sacrum* ferredoxins, have been carried out by means of X-ray method. This thesis consists of a study on *Spirulina platensis* ferredoxin analyzed at 2.8 Å resolution and that on *Aphanothece sacrum* ferredoxin at 5 Å resolution.

Table I-1. Comparison of physicochemical properties of both types of ferredoxins

	Bacterial type		Chloroplast type
	anaerobic	photosynthetic	
Absorption maxima (oxidized form)	280,390	280,310,385	277,331,422,465
Molecular weight	6,000	9,000	11,500
Number of non-heme iron atoms	8	4	2
Number of cysteine residues	8	4	5
Number of inorganic sulfur atoms	8	4	2
Oxidation-reduction potential	-410 mV	-490 mV	-420 mV
Reducing equivalent per mole	2	1	1
Number of residues	55	81	97

The properties given in this table of anaerobic bacterial type are represented by *Clostridial* ferredoxin (1), that of photosynthetic bacterial type by *Chromatium* ferredoxin (30,31), and that of chloroplast type by alfalfa ferredoxin (32). Recent study discovered the ferredoxins not classified in these types properly. In this thesis, for the sake of convenience, the ferredoxin having a 4Fe-4S* cluster is called as photosynthetic bacterial ferredoxin, whether the organism has the function of photosynthesis or not, and that having two 4Fe-4S* clusters merely as bacterial one.

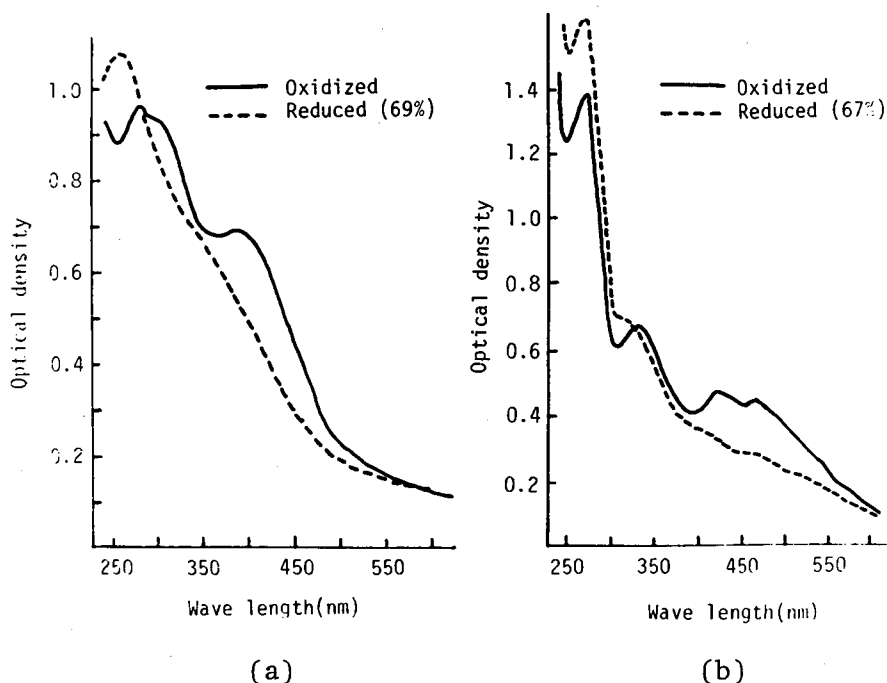


Fig. I-1. Absorption spectra of (a) *Clostridium* ferredoxin and (b) spinach ferredoxin (4).

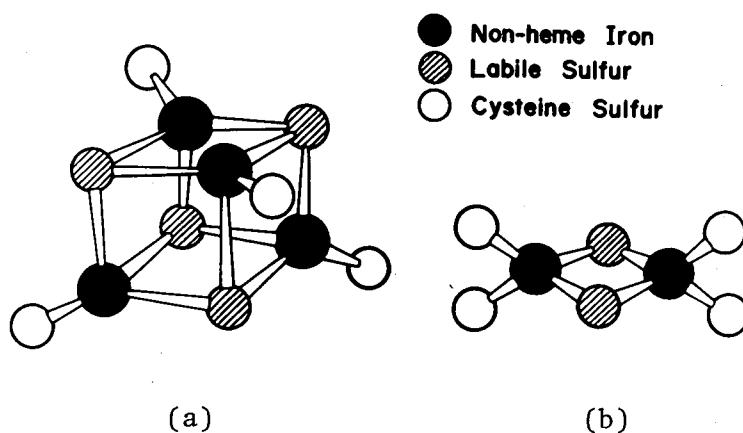


Fig. I-2. Structures of the clusters of (a) bacterial ferredoxin (8) and (b) chloroplast type one (suggested) (33,34).

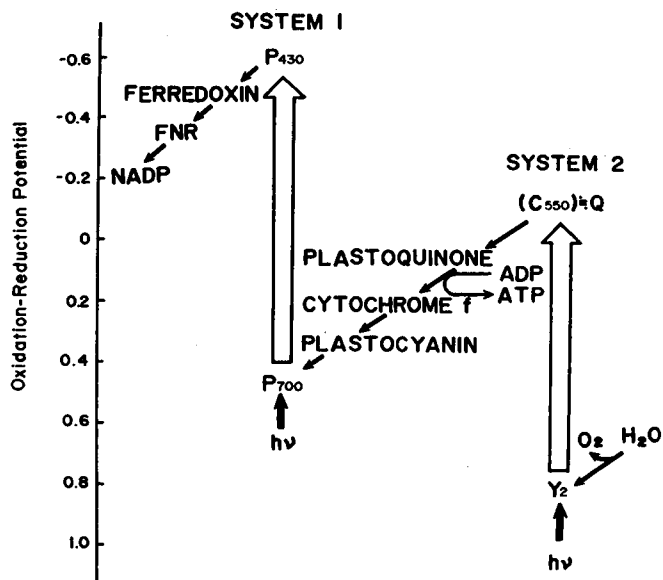


Fig. I-3. Electron transfer system in photosynthesis.

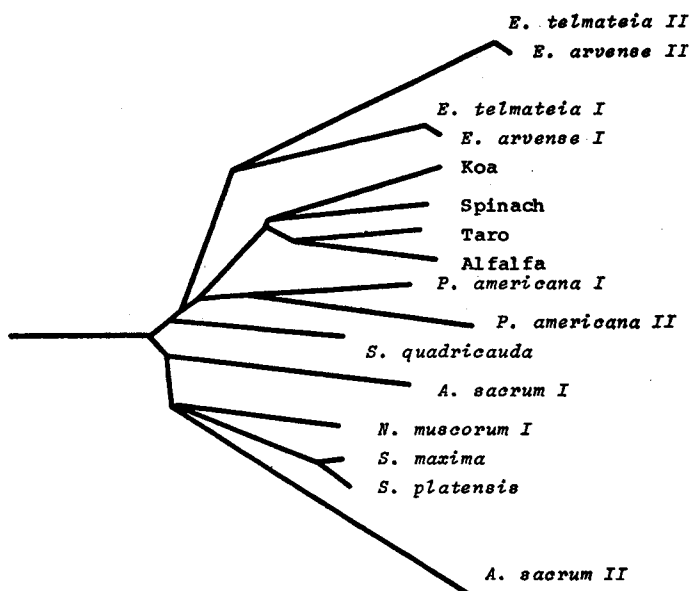


Fig. I-4. Phylogenetic tree of chloroplast type ferredoxins (27).

	10	20	30	40
(A) Taro	ATYKVKLVLT	-PSG-QQEFQCPDDVYILDQAEEV	GIDLPYSC	RAGS
(B) Koa	-AFKVKLLT	-PDG-PKEFEC	PDDVYILDQAEE	LGIDLPYSC
(C) Spinach	AAYKVT	LVLT-PTG-NVEFQCPDDVYILD	AAEEEGIDLPYSC	RAGS
(D) Alfalfa	ASYKVKLVLT	-PEG-TQEFEC	PDDVYILDHAEEEGIVLPYSC	RAGS
(E) P. americana I	ATYKVT	LVLT-PSG-TQTIDCPDDTYVLDA	AAEEAGLDLPYSC	RAGS
(F) P. americana II	ASYKVT	FVLT-PSG-TNTITCPADTYVLDA	AAEESGLDLPYSC	RAGA
(G) E. telmateia I	-AYKTVLKT	-PSG-EFTLDVPEGTTILDA	AAEEAGYDLPPFSC	RAGA
(H) E. telmateia II	-AYKVT	LKT-PDG-DITFDVEFGERLIDIA	SEKA-DLPLSC	QAGA
(I) E. arvense I	-AYKTVLKT	-PSG-EFTLDVPEGTTILDA	AAEEAGYDLPPFSC	RAGA
(J) E. arvense II	-AYKVT	LKT-PDG-DITFDVEFGERLIDIG	SEKA-DLPLSC	QAGA
(K) S. quadricauda	ATYKVT	LKT-PSG-DQTIECPDDTYILDA	AAEEAGLDLPYSC	RAGA
(L) A. sacrum I	ASYKVT	LKT-PDG-DNVITVPDDEYILD	VAAEEEGLDLPYSC	RAGA
(M) A. sacrum II	ATYKVT	LINEEEEGINAILEVADDQTI	LDAGEEAGLDLPSS	CRAGS
(N) S. platensis	ATYKVT	LINEAEGINETIDCDDDTYILDA	AAEEAGLDLPYSC	RAGA
(O) S. maxima	ATYKVT	LISEAEGINETIDCDDDTYILDA	AAEEAGLDLPYSC	RAGA
(P) N. muscorum I	ATFKVT	LINEAEGTKHEIEVDPDEYILD	AAEEEGYDLPPFSC	RAGA

	50	60	70	80	90	100
(A) CSSCAGKVKVGDV	-DQSDGSFLDDDEQ	IGEGWVLT	CVAYPVSDGT	IE	THKEEEL	TA
(B) CSSCAGKLVEGDL	-DQSDQSFLDDDEQ	IEEGWVLT	CAAYPRSDV	VIETHKEEEL	TG	
(C) CSSCAGKLKTGSL	-NQDDQSFLDDDDQ	IDEGWVLT	CAAYPVSDV	TIETHKEEEL	TA	
(D) CSSCAGKVAAGEV	-NQSDGSFLDDDDQ	IEEGWVLT	CVAYAKSDV	TIETHKEEEL	TA	
(E) CSSCTGKV	TAGTV-DQEDQSFLDDDDQ	IEAGFVLT	CVAFPKGDV	TIETHKEEDIV		
(F) CSSCAGKV	TAGAV-NQEDGSFL	EEEQMEAGWVLT	CVAYPTSDV	TIETHKEEDLTA		
(G) CSSCLGKV	VSGSV-DQSEGSFLDDG	QMEEGFVLT	CI	AIPESDLVIETHKEEELF		
(H) CSTCLGKIV	SGTV-DQSEGSFLDDQ	IEQGYVLT	CI	AIPESDVVIETHKEDEL--		
(I) CSSCLGKV	VSGSV-DESEGSFLDDG	QMEEGFVLT	CI	AIPESDLVIETHKEEELF		
(J) CSTCLGKIV	SGTV-DQSEGSFLDDQ	IEQGYVLT	CI	AIPESDVVIETHKEDEL--		
(K) CSSCAGKVE	AGTV-DQSDQSFLDDDS	QMDGGFVLT	CVAYPTSDCTI	ATHKEEDLDF		
(L) CSTCAGKLV	SGPAPD-EDQSFLDDDDQ	IQAGYILT	CVAYPTGDC	VIETHKEEALY		
(M) CSTCAGKLV	SGAAPNQDDQAF	LLDDQLAAGWVMT	CVAYPTGDC	TIMTHQEESEVL		
(N) CSTCAGTIT	SGTI-DQSDQSFLDDDDQ	IEAGYVLT	CVAYPTSDCTI	KTHQEEGLY		
(O) CSTCAGKIT	SGSI-DQSDQSFLDDDDQ	IEAGYVLT	CVAYPTSDCTI	QTHQEEGLY		
(P) CSTCAGKLV	SGTV-DQSDQSFLDDDDQ	IEAGYVLT	CVAYPTSDVVI	QTHKEEDLY		

Table I-2. Sequences of chloroplast type ferredoxins (27).

II. Crystal structure analysis of *Spirulina platensis* ferredoxin

II-1. Experimental

Crystallization of the protein. The ferredoxin was extracted with a dilute Tris-HCl buffer, and purified by the DEAE-cellulose column chromatography and fractionation with ammonium sulfate (35,36). The purity of the ferredoxin is indicated by the ratio of absorbances at 422 and 275 nm ($R=A_{422}/A_{275}$) (35). The solution purified to the R value of 0.53 was used for crystallization. The protein solution of 1-3 % concentration was dialyzed at 3°C against 87 % saturated ammonium sulfate solution containing 0.5 M NaCl adjusted to pH 7.5 by 0.1 M Tris-HCl buffer. Before the dialysis, nitrogen gas was passed through the solution to displace the oxygen gas dissolved. After 5-20 days brown thin-plate crystals grew to the maximum size of 3 mm in width (Fig. II-1).

Crystal data. The crystal was sealed in glass capillary with mother liquor. The precession photographs (Fig. II-2) showed the crystal to be orthorhombic, space group $C222_1$, and also showed that X-ray diffractions out to about 2.5 Å resolution were measurable. The unit cell dimensions were refined by least-squares treatment of setting angles measured by four-circle diffractometer to be $a=62.32$, $b=28.51$, $c=108.08$ Å. The density of the crystal was measured by floatation method in 85 % saturated

ammonium sulfate solution containing cesium chloride. The molecular weight was calculated from the amino acid composition to be 10,648, including iron and inorganic sulfur atoms. Assuming the unit cell contains eight molecules, the crystal volume per unit of molecular weight, V_M , is calculated to be $2.25 \text{ \AA}^3/\text{dalton}$, which is reasonable compared with the values for various proteins tabulated by Matthews (37). The amino acid sequence and crystal data of the present protein are shown in Tables II-1 and II-2.

Preparation of heavy atom derivatives. At least two kinds of isomorphous heavy atom derivatives are generally required to solve the phase problem of protein structure by isomorphous replacement method. The heavy atom derivatives were prepared by the soaking method. The soaking solution was prepared by dissolving ammonium sulfate to a concentration of 85 % saturated, and was adjusted to pH 7.5 with Tris-HCl buffer. Each heavy atom reagent was dissolved in the solution. Before the soaking of the crystal, nitrogen gas was passed through the solution. The crystals were soaked in each solution at $2-4^\circ\text{C}$. The intensities of ($h00$), ($0k0$), and ($00l$) reflections of the soaked crystal were compared with those of the native crystal on a four-circle diffractometer. Instability of the crystal for heavy atom reagents made the preparation of the derivatives difficult. After an attempt for more than 30 reagents, the crystals soaked in $\text{K}_3\text{UO}_2\text{F}_5$, DyCl_3 , and YbCl_3 solutions were found to show reasonable changes

in the intensity distributions. However, the crystal soaked in YbCl_3 solution showed apparently identical in intensity distribution with that soaked in DyCl_3 solution. Therefore, the crystals soaked in $\text{K}_3\text{UO}_2\text{F}_5$ and DyCl_3 solutions were subjected to further intensity measurement. The intensity distributions of both derivatives are compared with those of the native crystal in Fig. II-3. The soaking conditions for each derivative are:

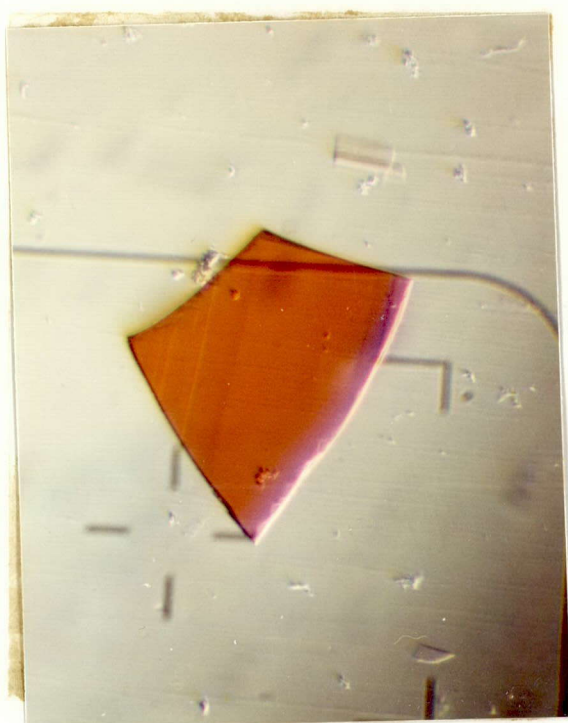
uranium derivative	52 mM	7 days
dysprosium derivative	44 mM	10 days.

Intensity measurement. The intensities of the native and derivative crystals were measured on a Rigaku computer-controlled four-circle diffractometer, equipped with a rotating anode X-ray generator, using Ni-filtered $\text{CuK}\alpha$ radiation. In order to utilize the phase information from anomalous scattering, the intensities of Bijvoet pair of reflections were measured, at (ϕ, χ, ω) for hkl and at $(\phi, \bar{\chi}, \omega)$ for $h\bar{k}l$, and as close together in time as possible. The air in the collimator and in the pathway from the crystal to the detector was evacuated to obtain high S/N ratio. Moving-crystal stationary-counter method was applied. In all the cases of the measurements the crystals were mounted with the b axis parallel to the ϕ axis of the diffractometer. The crystal was cooled to about $10\text{-}12^\circ\text{C}$ throughout the experiment to decrease its radiation damage. Experimental conditions for each measurement are summarized in Table II-3.

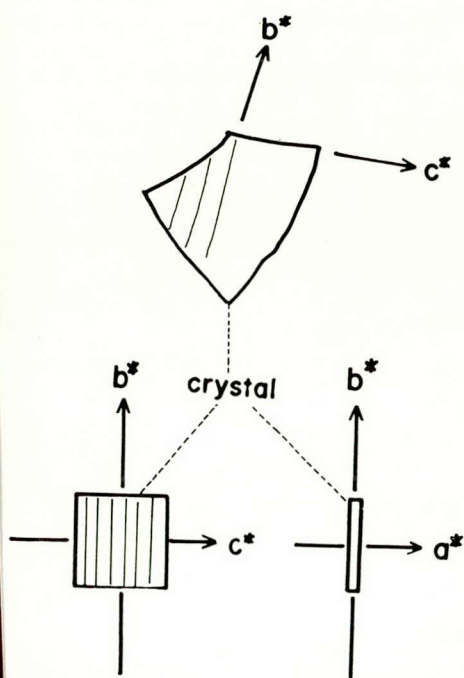
Data correction. Although the radiation damage was decreased to some extent by cooling the crystals, the damage was significant yet. The intensity-changes of monitor reflections of one crystal are shown in Fig. II-4, and F_E/F_S plots in Fig. II-5, where F_E and F_S represent the structure factors observed at the end and beginning of the measurement, respectively. The correction for radiation damage was made as functions of both exposure time and reflection angle (38). Since the shape of the crystal was thin plate, the change of intensities according to the azimuthal rotation was relatively large (Fig. II-6). The absorption correction was made by the method described by North *et al.* (39).

The (χ, ϕ) plots of $F(+)/F(-)$ were examined to detect any systematic error in Bijvoet differences. The plots for N-2, U-4, D-1, and D-2 data sets showed that the ratio $F(+)/F(-)$ deviated significantly from 1.0 as the χ -value deviated from zero. Therefore, these data were corrected as a function of χ assuming the ratio and χ -value have a linear relation.

The statistics for each data set are given in Table II-4 together with the relative scale and fall-off factors determined by Wilson's method (40). The reproducibility of the Bijvoet measurements is shown in Fig. II-7. The intensities of equivalent reflections measured from different crystals were averaged. The statistics of mean structure factors for 100-3.5 Å and 3.5-2.8 Å spacings are given in Table II-5.

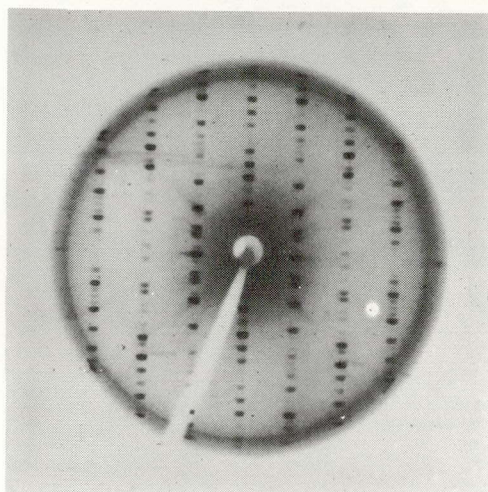


(a)

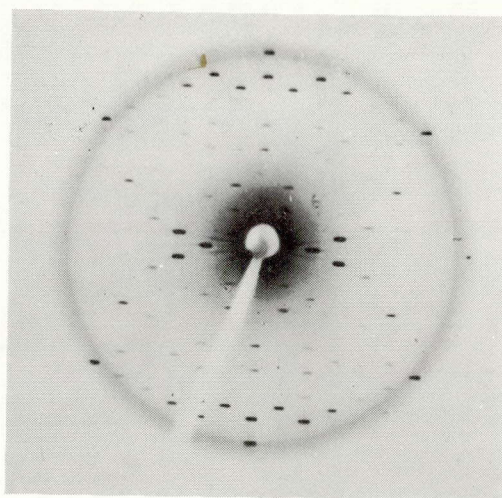


(b)

Fig. II-1. (a) Crystal of *Spirulina platensis* ferredoxin and (b) the schematic drawing of its external form.



(a)



(b)

Fig. II-2. Precession photographs of (a) the $(0kl)$ zone and (b) the $(hk0)$ zone of the native crystal of *Spirulina platensis* ferredoxin.

Table II-1. Amino acid sequence of *Spirulina platensis* ferredoxin (35).

1	5	10	15
Ala-Thr-Tyr-Lys-Val-Thr-Leu-Ile-Asp-Glu-Ala-Glu-Gly-Ile-Asn-			
16	20	25	30
Glu-Thr-Ile-Asp-Cys-Asp-Asp-Asp-Thr-Tyr-Ile-Leu-Asp-Ala-Ala-			
31	35	40	45
Glu-Glu-Ala-Gly-Leu-Asp-Leu-Pro-Tyr-Ser-Cys-Arg-Ala-Gly-Ala-			
46	50	55	60
Cys-Ser-Thr-Cys-Ala-Gly-Thr-Ile-Thr-Ser-Gly-Thr-Ile-Asp-Gln-			
61	65	70	75
Ser-Asp-Gln-Ser-Phe-Leu-Asp-Asp-Asp-Gln-Ile-Glu-Ala-Gly-Tyr-			
76	80	85	90
Val-Leu-Thr-Cys-Val-Ala-Tyr-Pro-Thr-Ser-Asp-Cys-Thr-Ile-Lys-			
91	95	98	
Thr-His-Gln-Glu-Glu-Gly-Leu-Tyr			

Table II-2. Crystal data.

Molecular formula	$C_{446}H_{684}O_{169}N_{110}S_8Fe_2$
Molecular weight	10,648
Space group	$C222_1$ (orthorhombic)
Cell dimensions: $a=62.32$, $b=28.51$, $c=108.08$ Å	
$V=1.920 \times 10^5$ Å ³ , $\rho_m=1.28$ g.cm ⁻³	
$Z=8$, $V_M=2.25$ Å ³ / dalton ^{a)}	

a) $V_M = V/ZM$, where V , Z , and M are the volume of unit cell, number of molecules in a unit cell, and molecular weight of the protein (37).

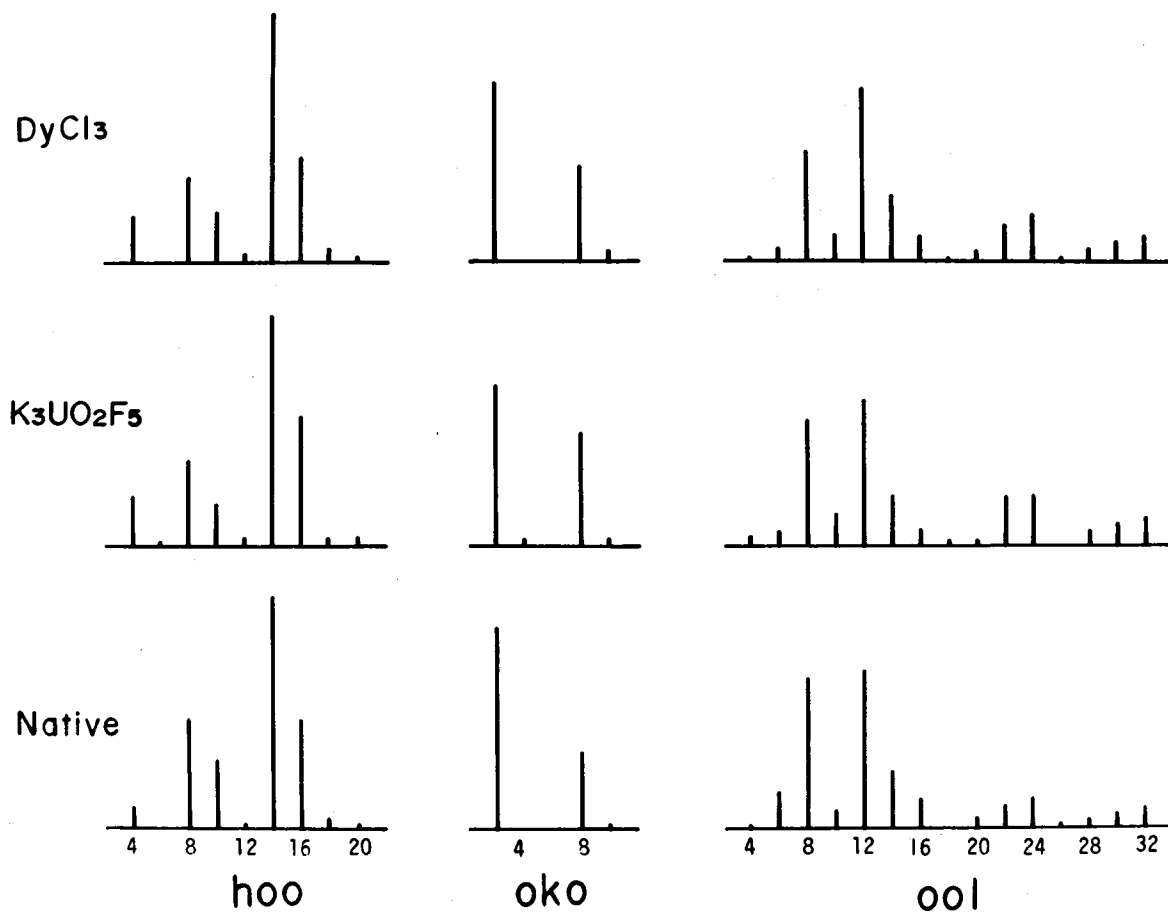


Fig. II-3. Schematic representation of diffraction profiles for native and derivative crystals along three crystallographic axes. Horizontal axis shows indices of each axis.

Table II-3. Experimental conditions of each data set for intensity measurement.

Crystal	Resolution	Scan speed	Background	Scan range	Radiation damage*	
	(Å)				(deg./min)	(seconds)
native						
N-1	100-2.8	4	5.0	$1.5+0.15\tan\theta$	0.80	-8.6
N-2	100-3.5	4	3.5	$1.4+0.15\tan\theta$	0.92	-3.6
N-3**	4.0-2.8	8	3.5	$1.2+0.15\tan\theta$	0.96	-3.0
U-derivative						
U-1	100-3.5	4	4.0	$1.4+0.15\tan\theta$	0.75	-10.0
U-2	100-3.5	4	3.5	$1.8+0.15\tan\theta$	0.90	-5.0
U-3	100-3.5	8	3.5	$1.8+0.15\tan\theta$	0.99	-2.0
U-4	4.0-2.8	8	3.2	$1.4+0.15\tan\theta$	0.96	-3.0
Dy-derivative						
D-1	100-3.5	4	3.0	$1.1+0.15\tan\theta$	0.91	-5.7
D-2	100-3.5	4	4.0	$1.5+0.15\tan\theta$	0.87	-4.4

*Radiation damage at the final stage of the measurement, and is represented in the form: $A+B(\sin\theta/\lambda)^2$.

**Not full set

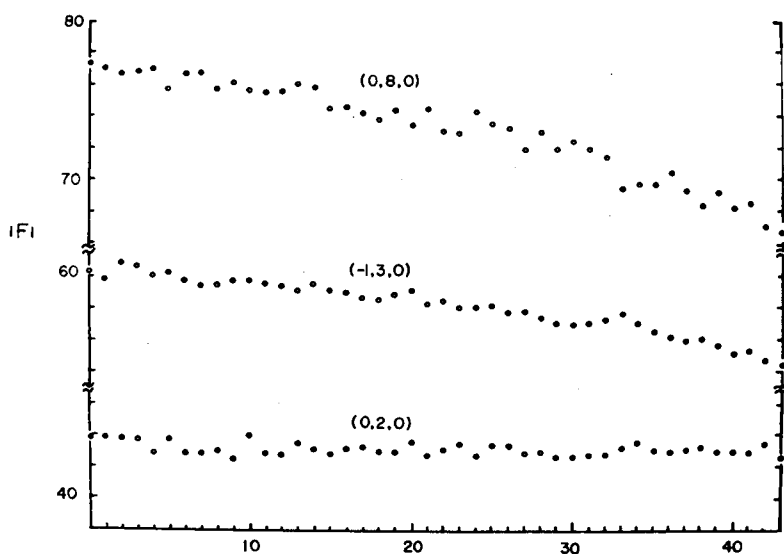


Fig. II-4. Changes of structure factors of monitor reflections of U-2 crystal, as an example. The measurements of their intensities were repeated every after about sixty structure factor measurements. $2\theta_{080}=24.97^\circ$, $2\theta_{-130}=9.41^\circ$, $2\theta_{020}=6.19^\circ$.

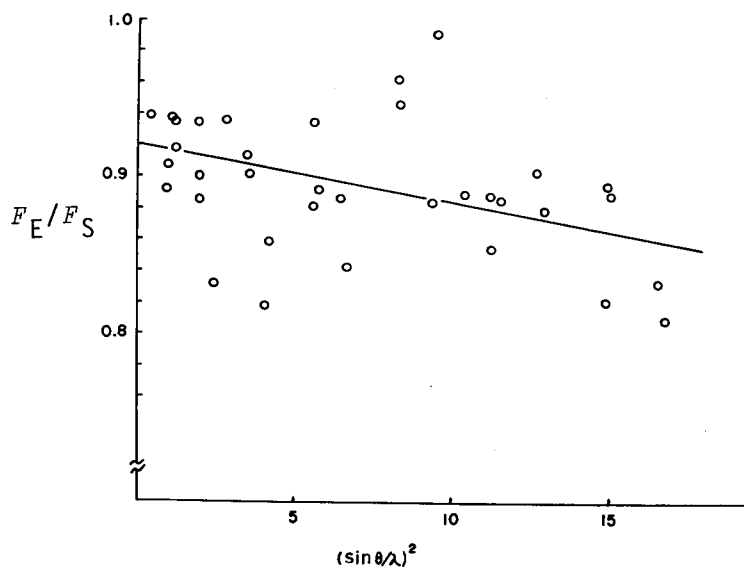


Fig. II-5. F_E/F_S plots of N-2 crystal, as an example, representing the dependence of radiation damage on reflection angle. The horizontal axis $(\sin \theta/\lambda)^2$ is multiplied by 10^3 .

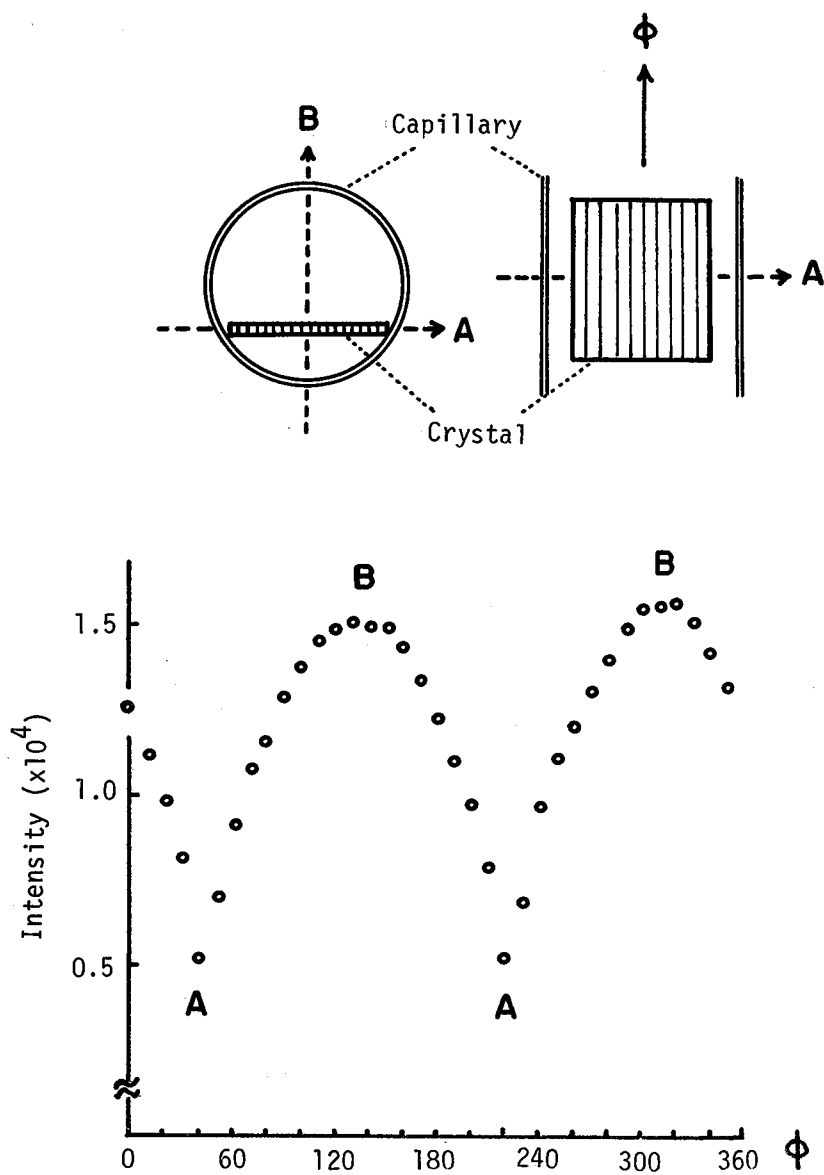


Fig. II-6. Change of intensities showing absorption of X-ray. The (0 2 0) reflection of N-1 crystal is shown as an example. The crystal was cut to rectangular form to facilitate the absorption correction.

Table II-4. Relative scale and fall-off factors and statistics of structure factors for each data set

Crystal	Δk	ΔB	$2\Sigma F(+)-F(-) / \Sigma \{F(+)+F(-)\}$	
			centric	non-centric
N-1	1.0	0.0	0.031 (92)	0.043 (854)
N-2	1.311	3.37	0.025 (69)	0.047 (603)
N-3	1.185	3.11	0.043 (14)	0.060 (258)
U-1	1.075	4.42	0.020 (70)	0.054 (657)
U-2	0.980	0.58	0.016 (69)	0.052 (638)
U-3	0.667	1.32	0.018 (58)	0.054 (766)
U-4	0.701	4.21	0.027 (37)	0.047 (436)
D-1	1.198	3.72	0.021 (67)	0.048 (691)
D-2	1.188	1.43	0.062 (62)	0.069 (617)

The relative scale and fall-off factors are in the form of $\Delta k \exp\{\Delta B(\sin\theta/\lambda)^2\}$, and were normalized to N-1. Numerals in brackets are the number of pairs of reflection included in calculation. The values for N-2, U-4, D-1, and D-2 are those after the correction against χ value (see text).

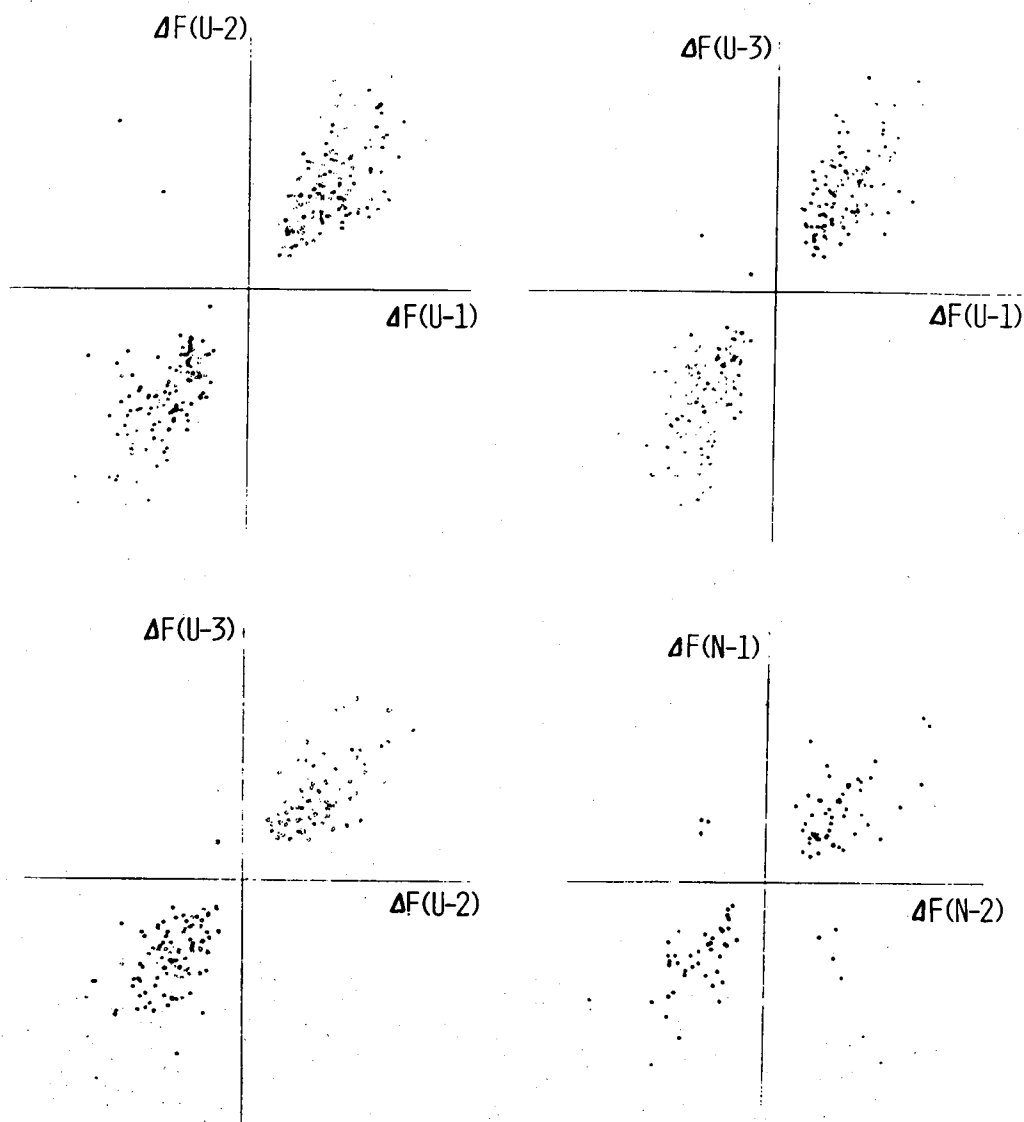


Fig. II-7. Plots of Bijvoet differences (ΔF) between two sets, representing reproducibility of the difference.

When the absolute of the difference ($|\Delta F|$) is greater than $\sigma(\Delta F)$, the corresponding plot is drawn.

Table II-5. Statistics between data sets and that for mean structure factors

(a)	i	j	$\Sigma \Delta F_{ij} / \Sigma \langle F_{ij} \rangle^a$	i	j	$\Sigma \Delta F_{ij} / \Sigma \langle F_{ij} \rangle$
	N-1	N-2	0.064	U-1	U-3	0.049
	N-1	N-3	0.084	U-2	U-3	0.045
	U-1	U-2	0.050	D-1	D-2	0.067

(b)	$\Sigma F_{PH} - F_P / \Sigma F_P ^b$
100-3.5 Å	0.137 (2394)
3.5-2.8 Å	0.137 (2003)

(c)	$2 \Sigma F(+) - F(-) / \Sigma \{F(+) + F(-)\}^c$			
	native		uranium derivative	
	centric	non-centric	centric	non-centric
100-3.5 Å	0.020 (76)	0.038 (684)	0.016 (90)	0.053 (803)
3.5-2.8 Å	0.067 (46)	0.075 (598)	0.045 (49)	0.078 (694)

a) The structure factors whose σ are less than 3.0 were used, except for the case of N-1-N-3 pair ($\sigma < 4.0$).

b) The structure factors having σ less than 4.0 are included in the calculation for 100-3.5 Å range, and those having σ less than 6.0 for 3.5-2.8 Å range. The numerals in bracket are the number of reflections involved.

c) The structure factors with $F > 10.0$ and $\sigma < 3.0$ were included for 100-3.5 Å range, and those with $F > 10.0$ and $\sigma < 6.0$ for 3.5-2.8 Å range.

II-2. Phase determination

Location of heavy atoms and refinement of their parameters. The principle of the difference Patterson function was described in detail by Blow (41) and Rossmann (42), and the function has been applied to locate heavy atoms in many protein crystals. The difference Patterson function was calculated to locate first the uranium atom with the coefficient of $(|F_{PH}| - |F_P|)^2$, where F_{PH} and F_P are the structure factors of the uranium derivative and native crystals, respectively. Two Harker sections of the function are given in Fig. II-8, which was interpreted as the derivative crystal to have a single heavy atom site with high occupancy. The parameters of the heavy atom were refined by the F_{HLE} method (43), which seems more favorable than the least-squares method described by Dickerson *et al.* (44) in the case that only one heavy atom derivative is available. The minimizing quantity was;

$$E = \sum w \{ k |F_{HLE}| \exp(\Delta B \sin^2 \theta / \lambda^2) - |f_H| \}^2,$$

where

w : weighting factor,

k : scale factor,

ΔB : relative fall-off factor,

$$F_{HLE}^2: |F_{PH}|^2 + |F_P|^2 - 2\{|F_P|^2 \cdot |F_{PH}|^2 - (k_{emp}/4)^2 (\Delta I)^2\}^{1/2},$$

f_H : calculated structure factor of the heavy atom.

The weighting factor for each reflection was given by $\{\sigma(F_{PH})^2 + \sigma(F_P)^2\}^{-1}$, and k_{emp} by 5.0 in this refinement. Since the occupancy of heavy atom in the crystal for U-4 data seemed to be different from that in the crystals for

the U-1, U-2, and U-3 data, the heavy atom parameters were refined independently. The difference Fourier synthesis with the coefficient of $(|F_{PH}| - |F_P|)\exp(i\alpha_P)$ showed no other prominent site (Fig. II-9). The final parameters of the heavy atom are listed in Table II-6.

The site of dysprosium atom was inspected by the difference Fourier synthesis with the coefficient of $(|F_{PH}| - |F_P|)\exp(i\alpha_P)$, where F_{PH} is the structure factor of the dysprosium derivative crystal, and α_P is the best phase angle determined by the uranium derivative (45). The major site of the dysprosium derivative was close to the uranium site of the uranium derivative, and a minor site was found. Since dysprosium atom has less anomalous scattering power than uranium atom and the F_{HLE} refinement for the dysprosium derivative did not proceed well compared with that for the uranium derivative, the dysprosium derivative was not used further to calculate the probability of the phase angles. Thus, the determination of the phase angles was obliged to base on the single isomorphous replacement method (46) coupled with the anomalous dispersion method (47).

Determination of absolute configuration and location of iron atoms. The enantiomorph of the protein structure must be chosen correctly. In the case of the multiple isomorphous replacement method, choice of the incorrect enantiomer of the heavy atom arrangement leads to only the incorrect enantiomer of the protein structure (which

consists of D-amino acid), so that no serious error will arise in the interpretation of the electron density map, and that the problem will be resolved by high resolution analysis. While in the case of the single isomorphous replacement method, anomalous dispersion data will give nonsense phase information if the enantiomer of the heavy atom arrangement is incorrectly chosen (Fig. II-10). Therefore, the determination of absolute configuration is quite important for application of the anomalous dispersion method based on the single isomorphous replacement method, particularly at the resolution where the protein structure can not be resolved at atomic level.

Fortunately, the present protein has two iron atoms, so that the absolute configuration could be determined by the difference Fourier technique utilizing their anomalous scattering (48). One prominent peak was found using 5 Å resolution data in the difference Fourier synthesis with the coefficient of $m\{|F_P(+)| - |F_P(-)|\} \exp\{i(\alpha_P - \pi/2)\}$, where $F_P(+)$ and $F_P(-)$ are structure factors of Bijvoet pair of the native crystal, α_P is the best phase angle determined by the single isomorphous replacement method, and m is the figure of merit (described later). In addition, the site showed high density in the best Fourier synthesis. Therefore, it was concluded that the site was a cluster consisted of two iron and two inorganic sulfur atoms, and that enantiomorph chosen was correct. This conclusion was confirmed by the difference Fourier synthesis with the coefficient of $m\{|F_{PH}(+)| - |F_{PH}(-)|\} \exp\{i(\alpha_P - \pi/2)\}$ which

showed a large peak at the same site as well as the uranium site.

The difference Fourier synthesis was calculated to locate individual iron atoms using 2.8 \AA resolution data with the coefficient of $m\{|F_P(+)| - |F_P(-)|\} \exp\{i(\alpha_P - \pi/2)\}$, where α_P was calculated from the single isomorphous replacement method coupled with the anomalous dispersion method. The peak was not completely resolved into two sites but revealed as elongated rod shape, however, the shape of the peak was consistent with the Fe-Fe distance being 2.7 \AA obtained from X-ray analysis of the analog (34). The sites of two iron atoms were assigned as (0.318, 0.054, 0.340) and (0.315, 0.125, 0.322) from a shape analysis of the peak. The difference map is shown in Fig. II-11. The ratio of peak height of maximum background to that corresponding to the cluster was about 0.6 at 2.8 \AA resolution.

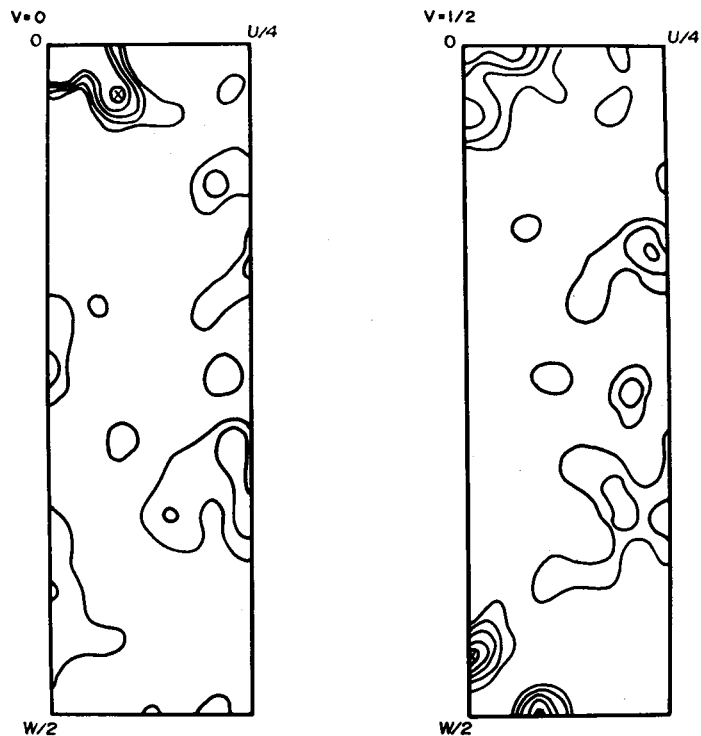


Fig. II-8. Difference Patterson function (uranium-native). Two Harker sections are shown in which cross marks indicate vectors between the heavy atoms.

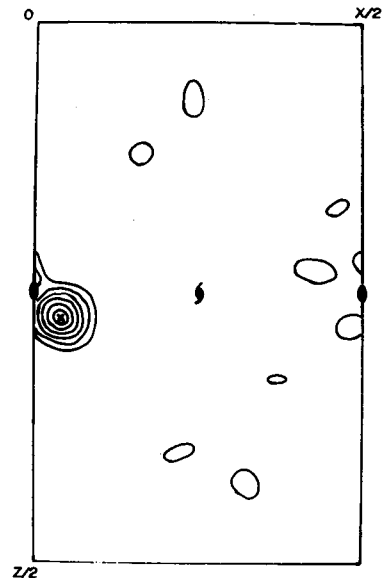


Fig. II-9. Difference Fourier synthesis (uranium-native). Section at $y=32/120$ is shown.

Table II-6. Heavy atom parameters of uranium derivative

	100-3.5 Å	3.5-2.8 Å
$G^a)$	30.9 (9)	33.3 (76)
x	0.0450 (4)	0.0475 (6)
y	0.2789 (11)	0.2790 (11)
z	0.2700 (2)	0.2701 (3)
B	23.8 (34)	16.3 (91)
$R^b)$	0.37	0.46

a) Effective occupancies in number of electrons.

b) $R = \sum |F_{\text{HLE}} - f_{\text{H}}| / \sum |F_{\text{HLE}}|$. In this F_{HLE} refinement, the 836 reflections with $F > 10$ and $\sigma < 2.5$ were used for 100-3.5 Å, and 436 reflections with $F > 10$ and $\sigma < 4.0$ for 3.5-2.8 Å.

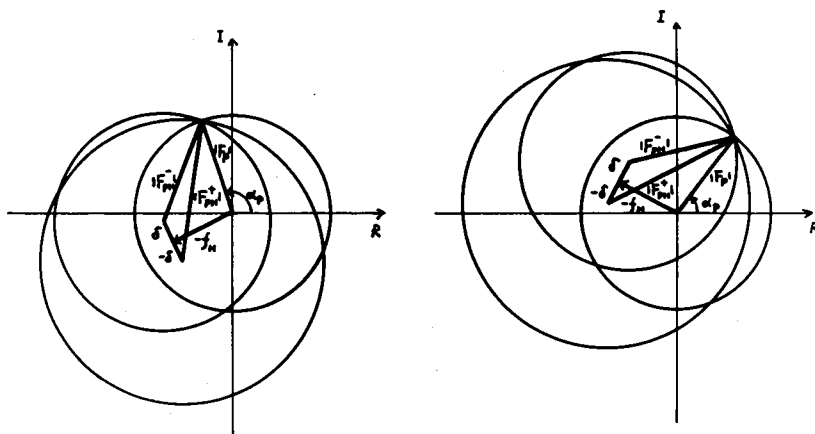


Fig. II-10. Phase diagram showing that incorrect choice of enantiomer of the heavy atoms leads to nonsense phase in the case of the single isomorphous replacement method coupled with the anomalous dispersion method.

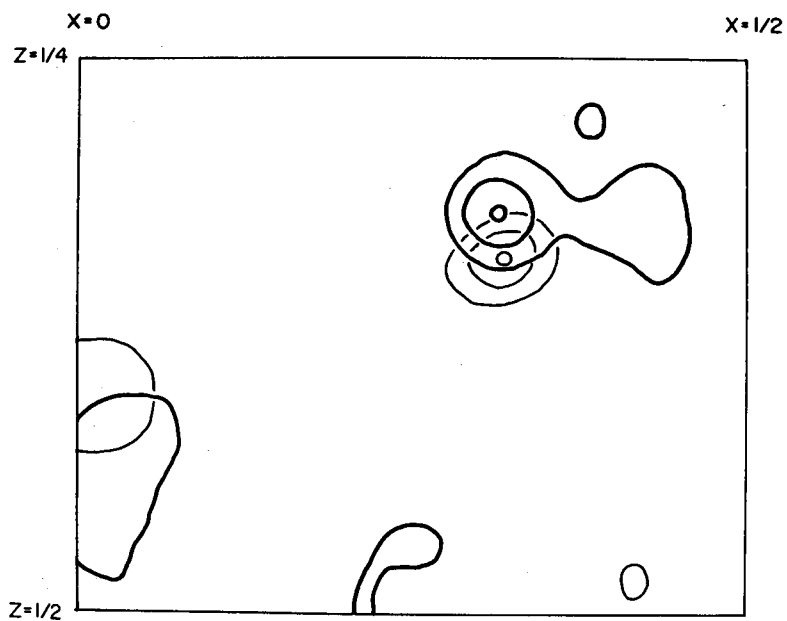


Fig. II-11. Anomalous difference Fourier synthesis at 2.8 \AA resolution. Two sections are superimposed; the bold lines indicate the contours at $y=16/120$, and thin lines those at $y=4/120$.

Calculation of electron density map. The best phase angle and the figure of merit of the native crystal were calculated according to the following equations (44).

$$m \cos(\alpha_p) = \int_0^{2\pi} P(\alpha) \cos(\alpha) d\alpha / \int_0^{2\pi} P(\alpha) d\alpha,$$

$$m \sin(\alpha_p) = \int_0^{2\pi} P(\alpha) \sin(\alpha) d\alpha / \int_0^{2\pi} P(\alpha) d\alpha,$$

where $P(\alpha)$ is the probability of phase angle α , and represented by $P(\alpha) = P_{\text{iso}}(\alpha) \cdot P_{\text{ano}}(\alpha) \cdot P_{\text{nano}}(\alpha)$. The probabilities, $P_{\text{iso}}(\alpha)$, $P_{\text{ano}}(\alpha)$, and $P_{\text{nano}}(\alpha)$, are calculated independently from the isomorphous replacement, anomalous dispersion, and native anomalous dispersion methods. Each of $P(\alpha)$'s has the general form;

$$P(\alpha) = \exp\{-\epsilon^2(\alpha)/2E^2\},$$

where $\epsilon(\alpha)$ is lack of closure, and E is rms error of ϵ .

In the present study, the method described by Hendrickson and Latteman (49) was adopted for representation of the phase probability distribution, $P(\alpha)$, which has the form;

$$P(\alpha) = N \exp(CK + A \cos \alpha + B \sin \alpha + C \cos 2\alpha + D \sin 2\alpha).$$

The coefficients for isomorphous case (49) were shown as;

$$CK_{\text{iso}} = -\{(F_P^2 + f_H^2 - F_{PH}^2)^2 + 2F_P^2 f_H^2\} / 2E^2,$$

$$A_{\text{iso}} = -2(F_P^2 + f_H^2 - F_{PH}^2) F_P a / E^2,$$

$$B_{\text{iso}} = -2(F_P^2 + f_H^2 - F_{PH}^2) F_P b / E^2,$$

$$C_{\text{iso}} = -F_P^2 (a^2 - b^2) / E^2,$$

and

$$D_{\text{iso}} = -2F_P^2 ab/E^2,$$

where a and b are real and imaginary components of the heavy atom contribution respectively. In the present case, E^2 was estimated to be $4f_H^2\{\sigma(F_P)^2 + \sigma(F_{PH})^2 + 2.0\}$, where $\sigma(F_P)$ and $\sigma(F_{PH})$ are counting statistics.

Since the present native protein contains anomalous scattering atoms (iron atom), the coefficients for anomalous case given in ref. 49 are no longer valid. The coefficients for such case have been modified as (Fig. II-12);

$$CK_{\text{ano}} = -\left\{ \left(\Delta H - \frac{2aa' + 2bb'}{F_{PH}} \right)^2 + \frac{2F_P^2(a'^2 + b'^2)}{F_{PH}^2} \right\} / 2E^2,$$

$$A_{\text{ano}} = \frac{2F_P a'}{F_{PH}} \left(\Delta H - \frac{2aa' + 2bb'}{F_{PH}} \right) / E^2,$$

$$B_{\text{ano}} = \frac{2F_P b'}{F_{PH}} \left(\Delta H - \frac{2aa' + 2bb'}{F_{PH}} \right) / E^2,$$

$$C_{\text{ano}} = -\frac{F_P^2}{F_{PH}^2} (a'^2 - b'^2) / E^2,$$

and

$$D_{\text{ano}} = -\frac{2F_P^2 a'b'}{F_{PH}^2} / E^2,$$

where ΔH is the observed Bijvoet difference of the derivative crystal, and a' and b' are real and imaginary components of total anomalous scattering, the anomalous scattering of the uranium and iron atoms in the present case.

The coefficients for native anomalous case have been derived as (Fig. II-13);

$$C_{\text{nano}}^{K} = -\{\Delta H'^2 + 2(\alpha''^2 + b''^2)\}/2E^2,$$

$$A_{\text{nano}} = 2\Delta H' \alpha''/E^2,$$

$$B_{\text{nano}} = 2\Delta H' b''/E^2,$$

$$C_{\text{nano}} = -(\alpha''^2 - b''^2)/E^2,$$

and

$$D_{\text{nano}} = -2\alpha'' b''/E^2,$$

where $\Delta H'$ is the observed Bijvoet difference of native crystal, and α'' and b'' are real and imaginary components of anomalous scattering of native crystal. For both anomalous cases, E^2 was estimated to be $\sigma(F_P)^2 + \sigma(F_{PH})^2 + 2.0$.

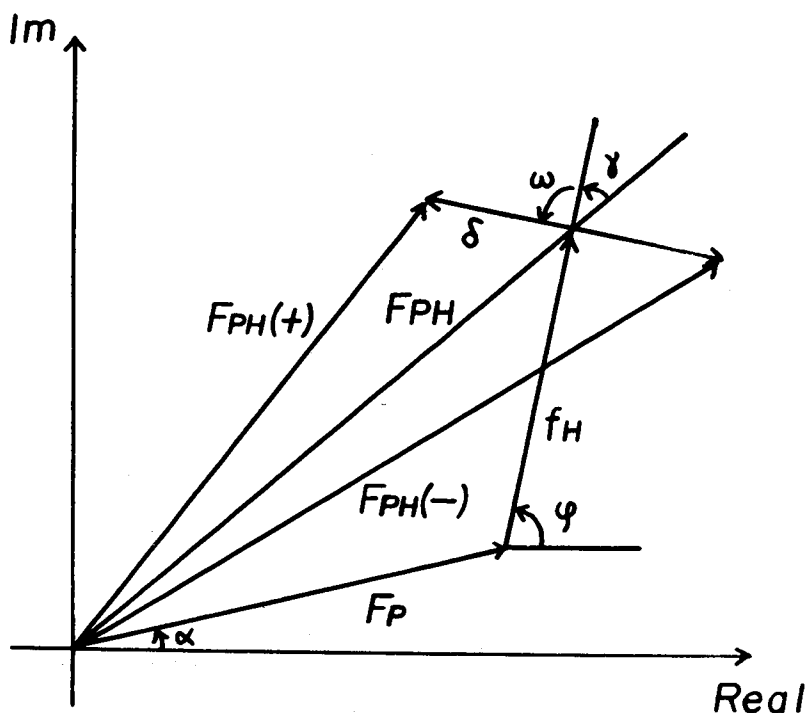


Fig. II-12. Phase diagram for anomalous case.

This protein has iron atoms having appreciable anomalous scattering power. In this case, the contribution of the heavy atom introduced by soaking, f_H , and total of anomalous scattering contribution in the derivative crystal, δ , are no more rectangular. Then, lack of closure error at given phase angle α , $\epsilon(\alpha)$, has been represented as (47);

$$\epsilon(\alpha) = \Delta H - 2\delta \cos(\gamma + \omega), \quad \dots \dots \dots (1)$$

where

$$\Delta H = |F_{PH}^{obs}(+)| - |F_{PH}^{obs}(-)|,$$

$$\sin \gamma = \{f_H^2 + F_P(b \cos \alpha - a \sin \alpha)\} / (F_{PH} f_H),$$

$$\cos \gamma = \{f_H^2 + F_P(a \cos \alpha + b \sin \alpha)\} / (F_{PH} f_H),$$

$$\sin \omega = (ab' - a'b) / (\delta f_H),$$

$$\cos\omega = (aa' + bb') / (\delta f_H).$$

The a , b , a' , and b' are $f_H \cos\phi$, $f_H \sin\phi$, $\delta \cos(\phi + \omega)$, and $\delta \sin(\phi + \omega)$, respectively. The second term of equation (1) is derived as;

$$\begin{aligned} \delta \cos(\gamma + \omega) &= \delta (\cos\gamma \cos\omega - \sin\gamma \sin\omega) \\ &= \frac{aa' + bb'}{F_{PH}} + \frac{F_P}{F_{PH}} (a' \cos\alpha + b' \sin\alpha). \end{aligned}$$

Thus the equation (1) becoms;

$$\epsilon(\alpha) = \Delta H - \frac{2F_P}{F_{PH}} (a' \cos\alpha + b' \sin\alpha) - \frac{2aa' + 2bb'}{F_{PH}}.$$

Then,

$$\begin{aligned} \epsilon^2(\alpha) &= \left(\Delta H - \frac{2aa' + 2bb'}{F_{PH}} \right)^2 - \frac{4F_P}{F_{PH}} (a' \cos\alpha + b' \sin\alpha) \left(\Delta H - \frac{2aa' + 2bb'}{F_{PH}} \right) \\ &\quad + \frac{4F_P^2}{F_{PH}^2} (a' \cos\alpha + b' \sin\alpha)^2. \end{aligned}$$

$$\begin{aligned} 2(a' \cos\alpha + b' \sin\alpha)^2 &= 2a'^2 \cos^2\alpha + 4a'b' \sin\alpha \cos\alpha + 2b'^2 \sin^2\alpha \\ &= (a'^2 - b'^2) \cos 2\alpha + 2a'b' \sin 2\alpha + (a'^2 + b'^2). \end{aligned}$$

Therefore,

$$\begin{aligned} -\epsilon^2(\alpha) / 2E^2 &= - \left\{ \left(\Delta H - \frac{2aa' + 2bb'}{F_{PH}} \right)^2 + \frac{2F_P^2 (a'^2 + b'^2)}{F_{PH}^2} \right\} / 2E^2 \\ &\quad + \frac{2F_P a'}{F_{PH}} \left(\Delta H - \frac{2aa' + 2bb'}{F_{PH}} \right) \cos\alpha / E^2 \\ &\quad + \frac{2F_P b'}{F_{PH}} \left(\Delta H - \frac{2aa' + 2bb'}{F_{PH}} \right) \sin\alpha / E^2 \\ &\quad - \frac{F_P^2}{F_{PH}^2} (a'^2 - b'^2) \cos 2\alpha / E^2 \\ &\quad - \frac{2F_P^2 a'b'}{F_{PH}^2} \sin 2\alpha / E^2. \end{aligned}$$

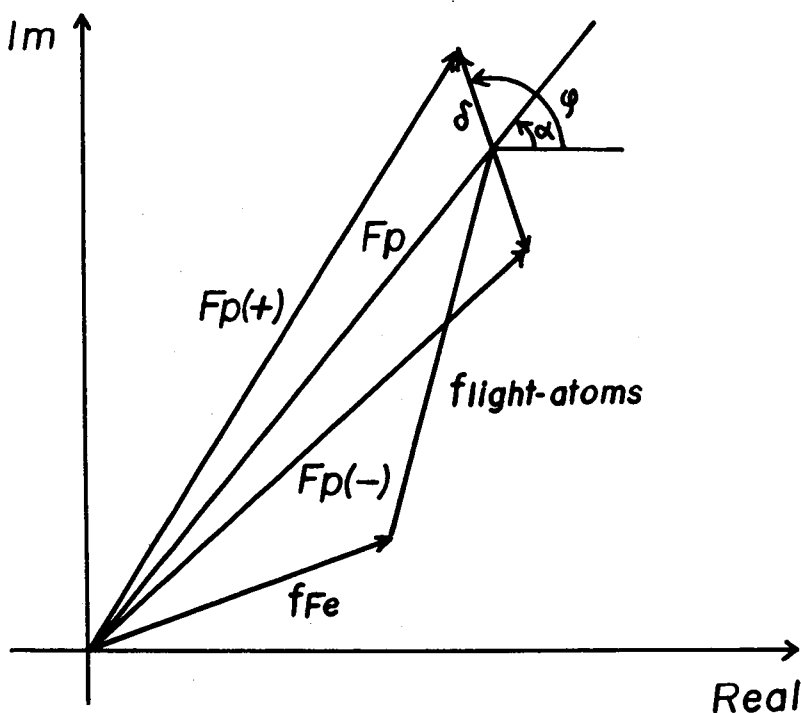


Fig. II-13. Phase diagram for native anomalous case.

Generally f_{Fe} is small compared with F_p , so that the calculated Bijvoet difference of the native crystal at a given phase angle α , ΔH_c , approximates to;

$$\begin{aligned}\Delta H_c &\approx 2\delta \cos(\phi - \alpha) \\ &= 2\delta (\cos\phi \cos\alpha + \sin\phi \sin\alpha) \\ &= 2(a'' \cos\alpha + b'' \sin\alpha),\end{aligned}$$

where δ is the anomalous scattering due to the iron atoms in the native crystal, $a'' = \delta \cos\phi$ and $b'' = \delta \sin\phi$. Therefore, the lack of closure error at the given phase angle α , $\epsilon(\alpha)$, becomes;

$$\begin{aligned}\epsilon(\alpha) &= \Delta H' - \Delta H_c \\ &= \Delta H' - 2(a'' \cos\alpha + b'' \sin\alpha),\end{aligned}$$

where $\Delta H'$ is the observed Bijvoet difference of the native crystal. Then,

$$\begin{aligned}
 \epsilon^2(\alpha) &= \Delta H'^2 - 4\Delta H'(a''\cos\alpha + b''\sin\alpha) + 4(a''\cos\alpha + b''\sin\alpha)^2 \\
 &= \Delta H'^2 - 4\Delta H'(a''\cos\alpha + b''\sin\alpha) \\
 &\quad + 4\{a''^2 \cdot \frac{1+\cos 2\alpha}{2} + a''b''\sin 2\alpha + b''^2 \cdot \frac{1-\cos 2\alpha}{2}\} \\
 &= \Delta H'^2 + 2(a''^2 + b''^2) - 4\Delta H'a''\cos\alpha - 4\Delta H'b''\sin\alpha \\
 &\quad + 2(a''^2 - b''^2)\cos 2\alpha + 4a''b''\sin 2\alpha.
 \end{aligned}$$

Thus,

$$\begin{aligned}
 -\epsilon^2(\alpha)/2E^2 &= -\{\Delta H'^2 + 2(a''^2 + b''^2)\}/2E^2 \\
 &\quad + (2\Delta H'a''/E^2)\cos\alpha \\
 &\quad + (2\Delta H'b''/E^2)\sin\alpha \\
 &\quad - \{(a''^2 - b''^2)/E^2\}\cos 2\alpha \\
 &\quad - (2a''b''/E^2)\sin 2\alpha.
 \end{aligned}$$

II-3. Interpretation of electron density map

Molecular model at low resolution. Electron density maps were calculated according to the following equation:

$$\rho(x,y,z) = (1/V) \sum_{hkl} m(hkl) |F_p(hkl)| \exp\{2\pi i(hx+ky+lz) + \alpha_p\},$$

where V is the volume of the unit cell of the crystal, and α_p is the best phase angle. The mean square error in electron density, $\langle(\Delta\rho)^2\rangle$, can be estimated by the following equation (44):

$$\langle(\Delta\rho)^2\rangle = (2/V^2) \sum_{hkl} |F(hkl)|^2 \{1 - m(hkl)\}^2.$$

In the early stage of structure analysis, the electron density map at 5 Å resolution was calculated in order to know the molecular packing mode in the crystal. The average figure of merit at this resolution was 0.76 for 364 reflections. The arrangement of the molecules is shown schematically in Fig. II-14. The wood model was made on the basis of the electron density map calculated at 3.8 Å resolution. The remarkable feature of the molecule ascertained at this analytical stage is that the cluster is close to the molecular surface, and that there is relatively large cavity at the opposite side of the cluster in the molecule.

Model building at 2.8 Å resolution. The electron density map at 2.8 Å resolution was calculated using 1736 reflections with the scale of 1 Å-2 cm. The average figure of merit and the root mean square error in electron density were estimated to be 0.49 and 0.07 e/Å³, respectively. The Kendrew type skeltal model was constructed using the

optical device described by Richards (50) which enable the electron density map and the model to be viewed simultaneously. The map was interpreted on the basis of the amino acid sequence determined by Wada *et al.* (35). The geometry of the cluster was assumed to be same as that of the analog of the present ferredoxin (34), and the bond lengths and angles in amino acid residues to have the well established values (51).

The molecular model construction was initiated from the region around the cluster. The positions of two iron atoms and the shape of the electron density distribution around the atoms enable to assign the orientation of the cluster. The segment from the Cys41 to the Cys49 could be fitted unambiguously to the electron density distribution around the cluster. The characteristic side chain of the Arg42 is clearly identified, and agreement of the model and the electron density around the cluster was excellent.

The model of other part of the chain, from the Ala50 to Cys79, from the Cys79 to C-terminal, and from the Cys41 to N-terminal, was successfully built up in this order. The model around N-terminal is less reliable, since the electron density corresponding to this region is low. The coordinates of alpha carbon atoms and the iron and sulfur atoms of the cluster are given in Table II-7.

There found some isolated peaks in the interior and near the surface of the molecule, especially at the bottom of the molecule. It was difficult to interpret them as a part of the molecule. They may be fixed solvent molecules.

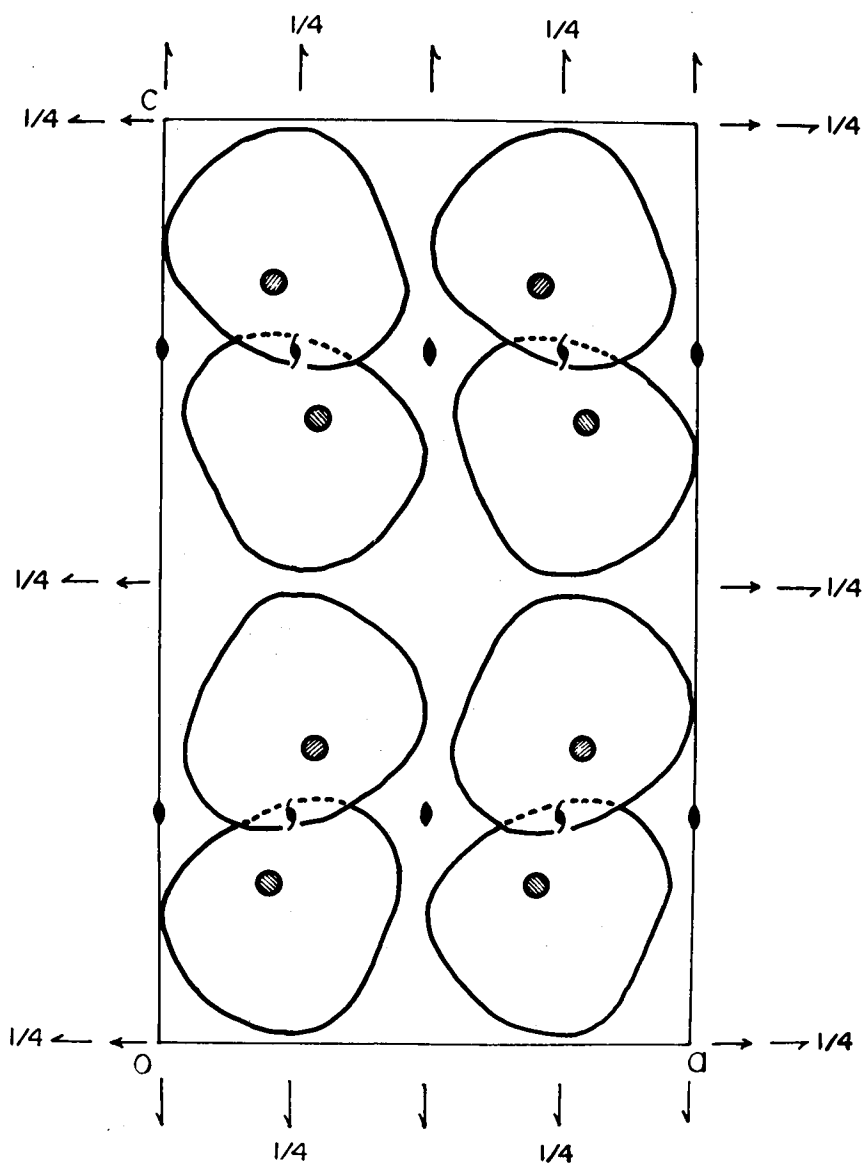


Fig. II-14. Schematic drawing of arrangement of the molecules. The shaded circle in each molecule shows the cluster. The molecules related by the 2_1 axis parallel to the b axis are closely contacted with one another at the neighbourhood of the cluster, while the region around the 2 axis parallel to the a axis ($y=1/2$) is filled with solvent.

Table II-7. Coordinates of the atoms of alpha carbon and
the cluster in Angstroms

	X	Y	Z		X	Y	Z
Ala1	8.19	-10.56	-7.12	Glu31	-17.57	-11.71	-16.75
Thr2	9.22	-7.89	-4.53	Glu32	-18.86	-14.41	-14.18
Tyr3	9.66	-10.24	-1.49	Ala33	-18.99	-11.44	-11.82
Lys4	8.12	-8.29	1.47	Gly34	-17.23	-12.67	-8.56
Val5	6.14	-10.58	3.89	Leu35	-16.40	-10.02	-5.82
Thr6	3.49	-12.46	1.77	Asp36	-13.09	-12.03	-5.35
Leu7	-0.03	-11.42	3.01	Leu37	-9.66	-10.24	-4.74
Ile8	-1.70	-11.55	-0.49	Pro38	-9.39	-6.36	-4.30
Asp9	-2.64	-14.96	-2.08	Tyr39	-8.16	-3.84	-7.04
Glu10	-6.49	-15.64	-1.60	Ser40	-8.94	-0.13	-5.99
Ala11	-7.56	-16.03	-5.32	Cys41	-6.20	1.79	-8.01
Glu12	-3.69	-16.11	-5.74	Arg42	-6.24	-0.76	-11.34
Gly13	-3.59	-18.04	-9.14	Ala43	-2.88	0.78	-12.16
Ile14	-3.45	-21.88	-9.84	Gly44	0.18	-1.87	-11.07
Asn15	-4.76	-22.01	-13.52	Ala45	1.13	0.67	-8.70
Glu16	-8.61	-22.17	-12.80	Cys46	-0.04	-1.32	-5.64
Thr17	-9.93	-20.08	-9.75	Ser47	-0.15	-4.96	-4.42
Ile18	-9.27	-21.23	-6.05	Thr48	-3.84	-5.15	-3.47
Asp19	-8.62	-21.19	-2.17	Cys49	-5.15	-6.81	-6.95
Cys20	-10.54	-22.28	1.10	Ala50	-2.15	-8.73	-5.93
Asp21	-14.11	-20.72	0.46	Gly51	-1.15	-12.32	-5.09
Asp22	-14.63	-19.54	-3.27	Thr52	-1.72	-14.82	-7.92
Asp23	-13.17	-21.86	-6.13	Ile53	1.10	-17.39	-8.02
Thr24	-14.10	-22.09	-9.98	Thr54	1.43	-19.50	-11.19
Tyr25	-11.56	-20.79	-12.76	Ser55	0.34	-23.05	-12.09
Ile26	-14.79	-20.32	-15.04	Gly56	-0.72	-23.32	-15.75
Leu27	-12.97	-16.78	-14.78	Thr57	2.75	-22.52	-17.14
Asp28	-12.60	-12.92	-14.59	Ile58	1.36	-19.33	-18.74
Ala29	-13.07	-9.46	-12.61	Asp59	3.22	-16.34	-17.25
Ala30	-16.71	-8.86	-14.10	Gln60	1.44	-13.06	-18.10

Table II-7. continued

	X	Y	Z		X	Y	Z
Ser61	1.94	-10.60	-20.99	Thr84	-0.56	-13.85	-22.91
Asp62	2.05	-6.83	-20.33	Ser85	0.73	-17.42	-22.86
Gln63	3.63	-6.69	-16.85	Asp86	-2.39	-19.48	-22.19
Ser64	2.61	-3.06	-16.13	Cys87	-4.85	-16.89	-23.47
Phe65	4.48	-2.40	-12.85	Thr88	-7.37	-19.73	-23.64
Leu66	5.63	-0.16	-9.95	Ile89	-9.30	-18.12	-26.49
Asp67	5.73	-2.77	-7.15	Lys90	-10.92	-14.75	-25.83
Asp68	6.38	-6.49	-7.83	Thr91	-9.22	-12.77	-23.07
Asp69	9.73	-4.63	-7.68	His92	-6.18	-12.66	-25.35
Gln70	12.01	-7.72	-7.87	Gln93	-5.13	-9.02	-25.05
Ile71	12.36	-11.50	-8.40	Glu94	-8.57	-7.40	-25.18
Glu72	8.64	-12.06	-9.86	Glu95	-8.78	-8.25	-21.48
Ala73	8.15	-15.70	-9.16	Gly96	-7.07	-9.87	-18.50
Gly74	4.68	-16.73	-7.88	Leu97	-8.07	-10.57	-14.90
Tyr75	2.69	-13.47	-8.28	Tyr98	-9.48	-7.29	-13.58
Val76	1.34	-11.04	-10.93	Fe1	-3.52	-1.76	-8.01
Leu77	-1.10	-8.18	-10.12	Fe2	-4.40	-3.27	-9.88
Thr78	-4.49	-9.08	-11.71	S*1	-5.53	-2.39	-8.26
Cys79	-6.29	-5.81	-12.52	S*2	-2.51	-2.52	-9.76
Val80	-3.60	-4.62	-15.41	S _Y 41	-3.28	0.54	-8.17
Ala81	-2.72	-7.81	-16.96	S _Y 46	-2.77	-2.18	-5.88
Tyr82	-4.00	-9.31	-20.21	S _Y 49	-5.26	-5.43	-9.44
Pro83	-2.54	-12.80	-19.84	S _Y 79	-5.46	-2.92	-12.18

The coordinates given in the table (X,Y,Z) are transformed to the crystallographic fractional coordinates (x,y,z) by the following equations:

$$x = -(X - 15.58) / 62.32,$$

$$y = (Y + 5.40) / 28.51,$$

$$z = -(Z - 27.02) / 108.08.$$

II-4. Description of structure of *Spirulina platensis* ferredoxin

Main chain folding. The molecule has approximate dimensions $40 \times 35 \times 25$ Å. The color photograph of the model is shown in Fig. II-15, and the stereoscopic view of the polypeptide chain drawn by PLUTO (52) in Fig. II-16. The cluster is located at the top of the molecule (colored by red in Fig. II-15) and near the surface of the molecule. Only the chain from the Cys41 to Cys46 covers the top-front side of the cluster. The top-rear side of the cluster, the sulfur atoms of the Cys41 and Cys46 and the iron atom coordinated by these sulfur atoms, is exposed to the environment. At the sight of Fig. II-15, it may be recognized that the upper half of the molecule consists mainly of hydrophobic residues (colored by yellow or orange) and that the lower half mainly of hydrophilic ones (colored by blue). The chain around the cluster folds relatively closely, while that at lower part of the molecule folds relatively loosely to have some cavities which may be filled with solvent. There appears to exist no α -helix in this protein. The chain from the Thr17 to Thr24 has a structure similar to antiparallel β -sheet structure. The structure of 3_{10} turn is found in this protein; CO(Asn9)----NH(Glu12), CO(Ile14)----NH(Thr17), CO(Asp19)----NH(Asp22), CO(Ala30)----NH(Ala33), CO(Tyr39)----NH(Arg42), and CO(Thr84)----NH(Cys87).

Heavy atom binding site. In the present protein, the side chains near the heavy atom site are those of the

Glu10 and Asp21. The Asp21 locates at a hair-pin loop of the antiparallel β -sheet which projects outside (lower left in Fig. II-16(b)). It is shown from protein structure so far studied that the heavy atom reagent, $K_3UO_2F_5$, generally binds to acidic side chain, Asp and Glu (38).

Chelate structure of active center. This protein involves six cysteinyl residues, of which the four, Cys41, Cys46, Cys49, and Cys79, are invariant residues. The present analysis has confirmed that the four cysteinyl sulfur atoms coordinate to the cluster. The Cys41 and Cys46 coordinate to one iron atom, and the Cys49 and Cys79 to the other iron atom. The chain folding around the cluster is shown in Fig. II-17. Although the structure of the cluster of chloroplast type ferredoxin ($2Fe-2S^*$) differs from that of bacterial type ferredoxin ($4Fe-4S^*$) (12), some similar features are found in the polypeptide chain around the cluster: two cysteinyl residues (Cys46 and Cys49) separated by two residues coordinate to different iron atoms, and only one cysteinyl residue, the Cys79, is comparatively apart from the other three cysteinyl residues in the amino acid sequence.

NH...S hydrogen bond. Inspection of the structure around the cluster showed some short contacts between nitrogen and sulfur atoms. These may be NH...S hydrogen bond, since in addition to the close contact each of the hydrogen atoms of NH is directed to the sulfur atom (53).

Adman *et al.* discussed the NH...S hydrogen bond around the clusters of bacterial ferredoxin, rubredoxin, and high-potential iron sulfur protein, and classified the bonds to four types according to their geometries. The geometries of types I and II are similar with those of 3_{10} NH...O hydrogen bonds. The acceptor of the hydrogen bond is a S_γ atom of a cysteinyl residue. The third type of the bond is such that the NH coordinates tetrahedrally around the S_γ atom, and the fourth type is such that the NH coordinates octahedrally to an inorganic sulfur atom. The geometries of the hydrogen bonds in the present ferredoxin are similar to those found in those proteins. The geometry of the chain from the sulfur atom of the Cys41 to the NH of the Ala43 is type I, and that from the sulfur atom of the Cys46 to the NH of the Thr48 type II. Although it has been suggested that the hydrogen bond exists between the NH of the Gly51 and the sulfur atom of the Cys49 from primary structures of chloroplast type ferredoxins (54), these groups appear to be too apart to interact with each other. Instead, the NH of the Cys79 appear to be close to the sulfur atom of the Cys49. The last hydrogen bond may play an important role to preserve the conformation of polypeptide chain around the cluster. It appears that there are some other approaches between sulfur atoms and NH groups.

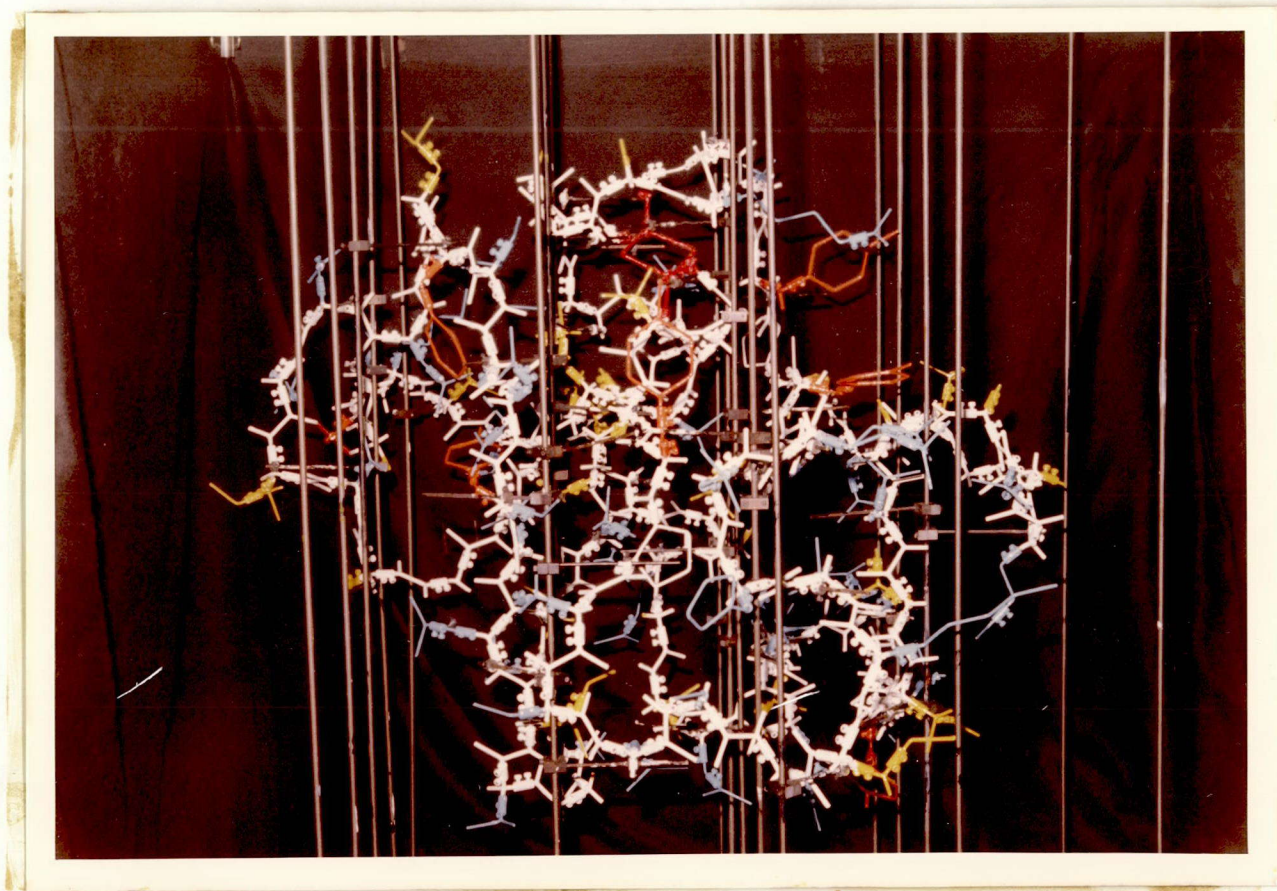
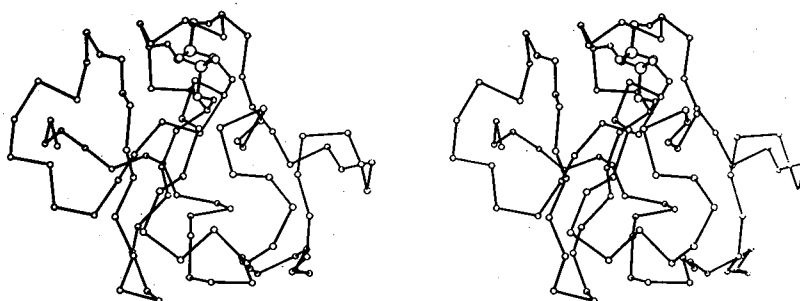
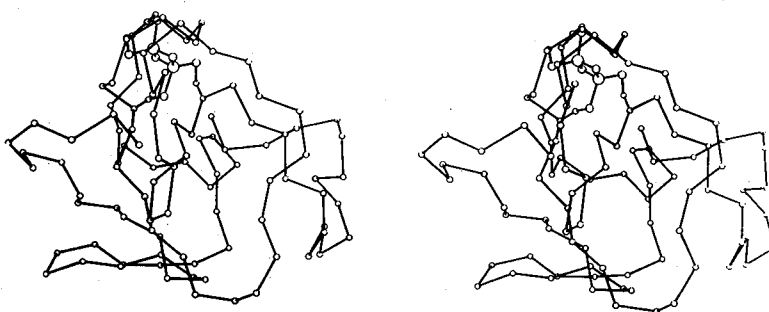


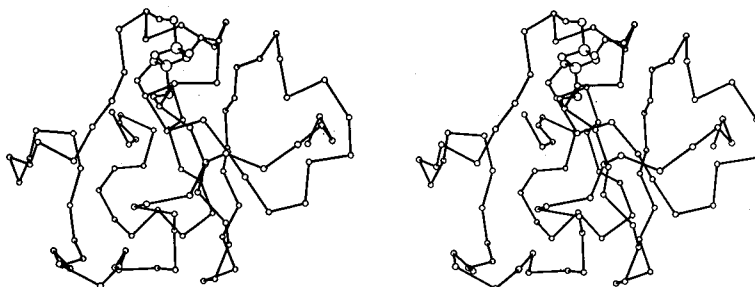
Fig. II-15. A color photograph of the molecular model of *Spirulina platensis* ferredoxin.



(a) Front view



(b) Side view



(c) Rear view

Fig. II-16. Folding of polypeptide chain shown by stereo-pair. Except for the cysteine residues coordinated to the iron atoms, only α -carbon of each residue is shown. View direction of (a) is the same as that in Fig. II-15.

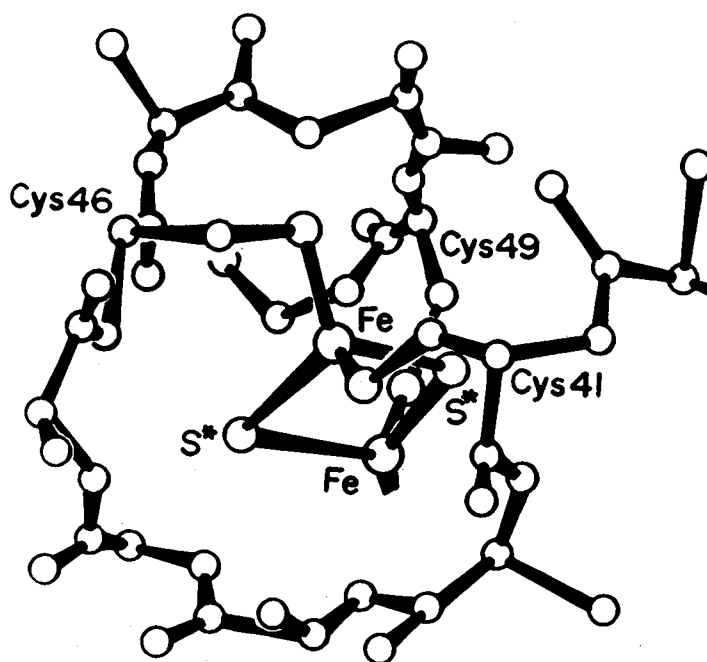


Fig. II-17. Chain folding around the cluster. Perspective drawing viewed from upper side of the molecule, in which the polypeptide chain from the α -carbon of Ser40 to that of Gly51 has been shown. Except for the cysteine, the atoms of γ, δ, \dots positions are omitted from the figure for the sake of clarity.

III. Crystal structure analysis of *Aphanothece sacrum* ferredoxin at 5 Å resolution

III-1. Experimental

Extraction, purification, and crystallization of the protein were carried out in the same manner with that of *Spirulina platensis* ferredoxin (35). The protein solution with the concentration of 1-3 % and with the A_{422}/A_{262} of 0.525 was dialyzed at 2-4°C against 75 % saturated ammonium sulfate solution containing 0.7 M NaCl adjusted to pH 7.5 by 0.1 M Tris-HCl buffer. After 15 days brown crystals in the form of dodecahedra grew to the maximum size of 0.8x0.8x0.4 mm. The microphotograph of the crystals and the schematic drawing of the external form are shown in Fig. III-1.

The precession photograph (Fig. III-2) showed the crystal to be tetragonal. The systematic absence of $h4n$ for (00 l) showed the space group to be $P4_1$ or $P4_3$ (the former was selected by means of anomalous dispersion technique described later). The unit cell constants were obtained by the least-squares method for 13 setting angles measured by a four-circle diffractometer. The density of the crystal was measured by floatation method in 85 % saturated ammonium sulfate solution containing cesium chloride. The V_M gives a reasonable value of 2.42 Å³/dalton (37), if the unit cell contains 16 molecules. Thus four molecules are involved in an asymmetric unit. The crystal data are shown in Table III-1.

The isomorphous heavy atom derivatives were prepared by the soaking method as the same way with that of *Spirulina platensis* ferredoxin. After screening of the heavy atom derivatives, the crystals soaked in $K_3UO_2F_5$, D_yCl_3 , and $K_2Pt(CN)_4$ solutions showed reasonable changes in the intensity distributions (Fig. III-3). The soaking conditions are:

uranium derivative	50 mM	10 days,
dysprosium derivative	61 mM	50 days,
platinum derivative	53 mM	5 days.

III-2. Intensity measurement

The crystal sealed in thin glass capillary was mounted with its c axis parallel to the ϕ axis of a Rigaku computer-controlled four-circle diffractometer. The intensities were measured using Ni-filtered $CuK\alpha$ radiation generated by rotating anode. The moving-crystal stationary-counter technique was adopted. The scan range varied from $0.7^\circ + 0.15^\circ \tan\theta$ to $1.2^\circ + 0.15^\circ \tan\theta$ according to crystals. The scan speed and background counting time at both sides of the scan range were $8^\circ/\text{min}$ and 2 seconds, respectively for each crystal. The air in the pathway of X-ray beam was also evacuated as the case for *S. platensis* ferredoxin. The intensities of hkl reflections were measured at (ϕ, χ, ω) and those of $h\bar{k}l$ reflections at $(\phi, \bar{\chi}, \omega)$.

The intensities up to 5 \AA resolution for the native crystal and the crystals of the uranium, dysprosium, and platinum derivatives were measured. The radiation damage

for the dysprosium derivative was serious. The damage for the platinum derivative was also serious, though the measurement for this derivative was made at 4°C. The radiation damage (in F) of 903 reflection ($2\theta=10.87^\circ$) at the end of the measurement was 5 % for the native crystal, 5 % for the uranium derivative crystal, 20 % for the dysprosium one, and 10 % for the platinum one.

The corrections for the radiation damage and absorption of the crystal (Fig. III-4) and the determination of relative scale and fall-off factors were made with the same way as that of *S. platensis* ferredoxin.

III-3. Phase determination

The difference Patterson function for the native and uranium derivative crystals showed two positions of the heavy atom sites. The Harker sections at $W=1/4$ and $W=1/2$ are shown in Fig. III-5. The parameters of the two heavy atoms were refined by the least-squares method. The difference Fourier synthesis with the coefficient of $(|F_{PH}| - |F_P|) \exp(i\alpha_P)$ showed no prominent peak other than the two peaks (Fig. III-6). Although four molecules are involved in an asymmetric unit, the heavy atom was introduced to only two sites. The final parameters of the heavy atom are given in Table III-3.

The difference Patterson function for the native and dysprosium derivative crystals or for the native and platinum derivative crystals could not be reasonably interpreted. Probably, this is due to rather inherent nature of each

derivative crystal, lack of isomorphism and/or multiple sites of the heavy atoms, than to serious radiation damage. Therefore, only the uranium derivative was used further for the phase determination.

The absolute configuration and the positions of the four clusters in an asymmetric unit were determined by the anomalous difference Fourier synthesis as applied for *S. platensis* ferredoxin. The map, which was calculated assuming the space group $P4_1$, clearly showed four prominent peaks as shown in Fig. III-7(a). The difference Fourier synthesis with the coefficient of $\{|F_{PH(+)}| - |F_{PH(-)}|\} \exp \{i(\alpha_P - \pi/2)\}$ also showed peaks corresponding to these positions as well as two uranium sites (Fig. III-7(b)). In addition these sites showed high density in the best Fourier map. Therefore the positions of the four clusters of the four molecules in an asymmetric unit were determined unambiguously. Consequently, the absolute configuration and the space group of $P4_1$ were also determined. The positions of the clusters are given in Table III-4 together with the peak heights found in the difference maps.

III-4. Molecular model at 5 Å resolution

The Fourier synthesis was calculated using the best phase angles determined by the single isomorphous replacement method coupled with the anomalous dispersion method for the derivative crystal. The mean figure of merit was 0.57 for 1291 reflections. The electron density map in a unit cell was drawn on a transparent sheet, and was

scrutinized to isolate the four crystallographically independent molecules from each other. The wood model made of polystyrene foam was constructed on the basis of the electron density map of a isolated molecule. The model is shown in Fig. III-8 by stereo-pair.

The molecule has approximate size of $36 \times 30 \times 25 \text{ \AA}$. The remarkable feature of the molecule is, as for *S. platensis* ferredoxin, that the cluster is located near the molecular surface and that there is a relatively large electron-density-deficient region at the interior of the molecule. The distances of two sets of the uranium atoms and the clusters, U(1) - (II) of 18.2 \AA and U(2) - (I) of 19.2 \AA (see Fig. III-7), are close with that found in *S. Platensis* ferredoxin. This fact suggests that the two molecules of the four crystallographically independent molecules catch the heavy atom at the same site with *S. platensis* ferredoxin.

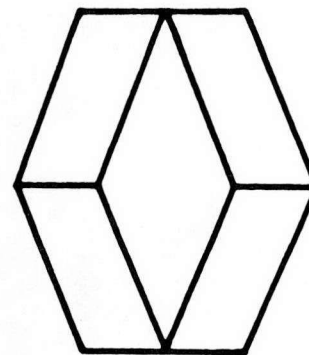
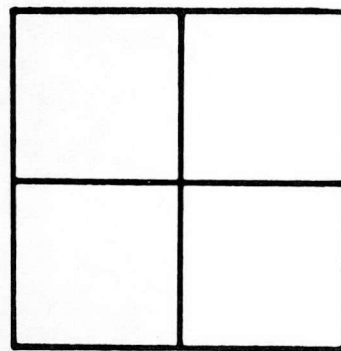
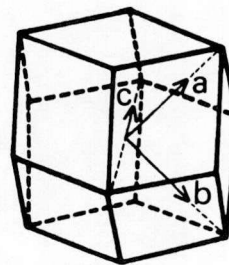
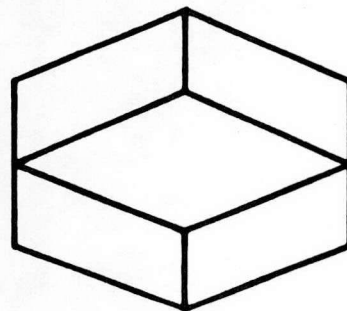
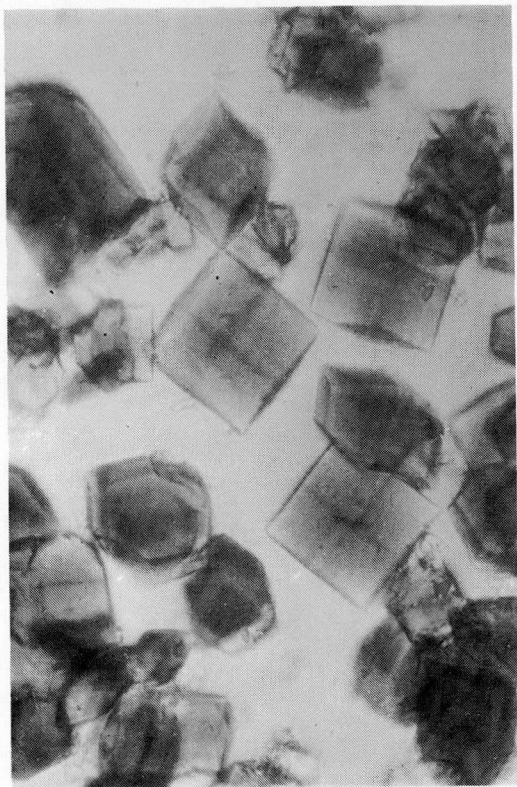


Fig. III-1. Crystals of *Aphanothece sacrum* ferredoxin, and schematic drawing of the external form.

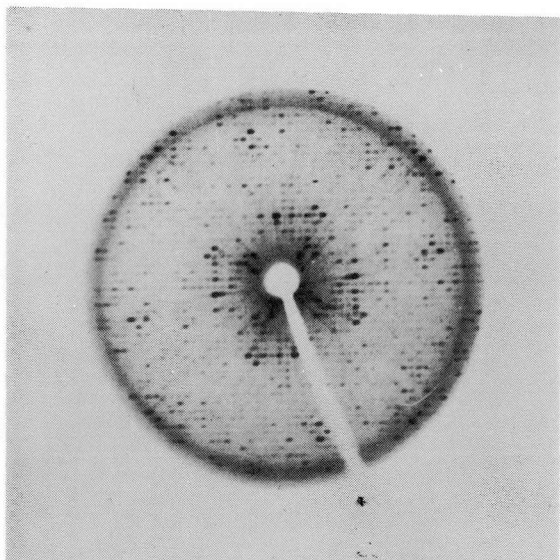


Fig. III-2. Precession photograph ($\mu=12^\circ$) of ($hk0$) zone showing four-fold symmetry.

Table III-1. Crystal data.

Molecular formula: $C_{448}H_{687}O_{159}N_{109}S_7Fe_2$

Molecular weight: 10,480

Space group: $P4_1$ (tetragonal)

Cell constants: $a=b=92.2$, $c=47.6 \text{ \AA}$

Volume of unit cell: $4.05 \times 10^5 \text{ \AA}^3$

Density of crystal observed: 1.27 g.cm^{-3}

Number of molecules in a unit cell: 16

$V_M = 2.42 \text{ \AA}^3/\text{dalton}$

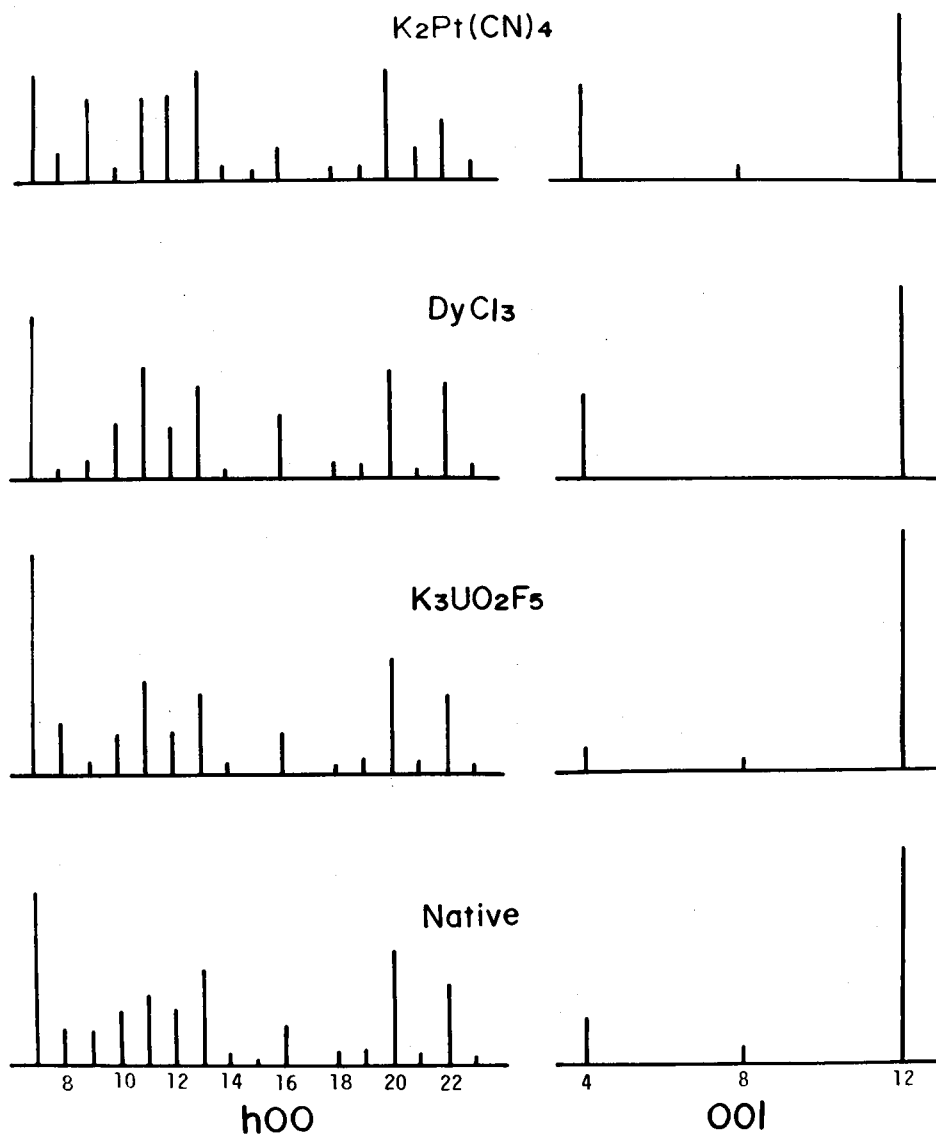


Fig. III-3. Schematic representation of diffraction profiles for native, uranium, dysprosium, and platinum derivative crystals. Horizontal axis shows indices of each axis.

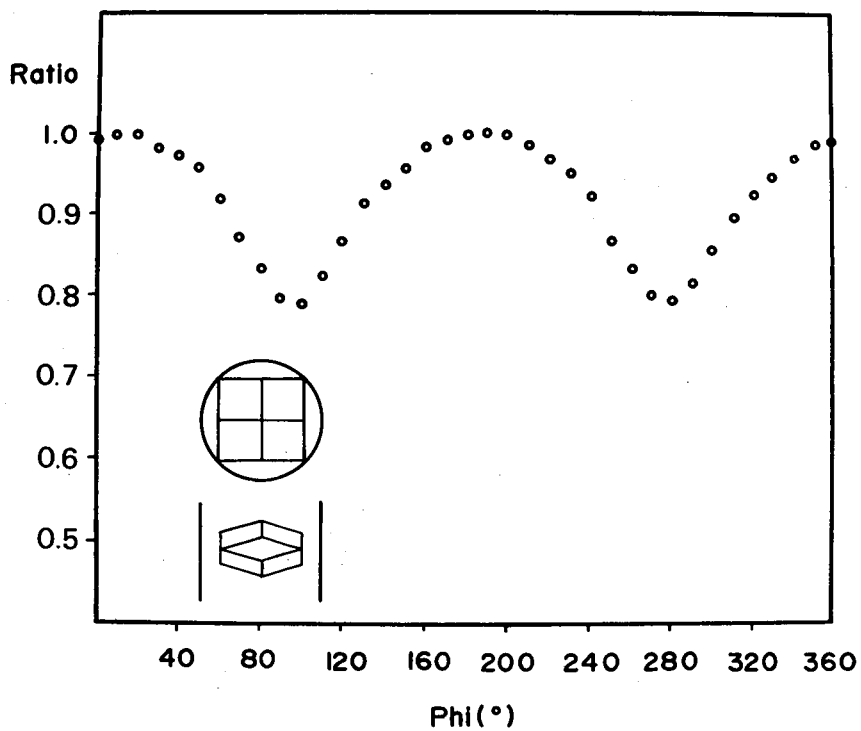


Fig. III-4. Variation of relative intensities with azimuthal angle ϕ .

Table III-2. Statistics of structure factors.

	native	U-derivative
$2\Sigma F(+)-F(-) /\Sigma \{F(+)+F(-)\}$	0.074	0.092
$2\Sigma F_{h0l}-F_{0kl} /\Sigma \{F_{h0l}+F_{0kl}\}$	0.058	0.098
$\Sigma F_{PH}-F_P /\Sigma F_P$		0.146
$\Sigma F_{PH}^2-F_P^2 /\Sigma F_P^2$		0.270

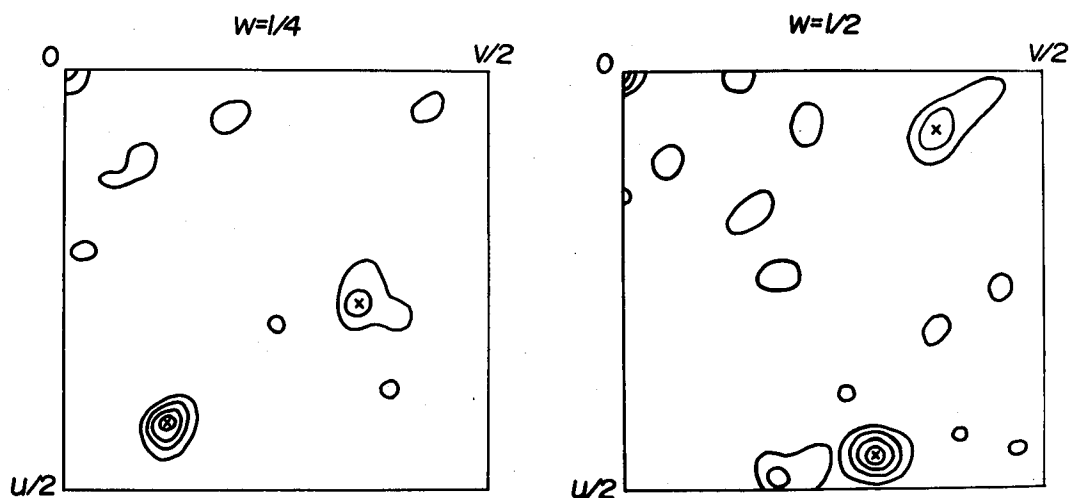


Fig. III-5. Difference Patterson function (uranium-native). Two Harker sections are shown, in which cross marks indicate vectors between the heavy atoms. These sections contain no cross vector between U1 and U2.

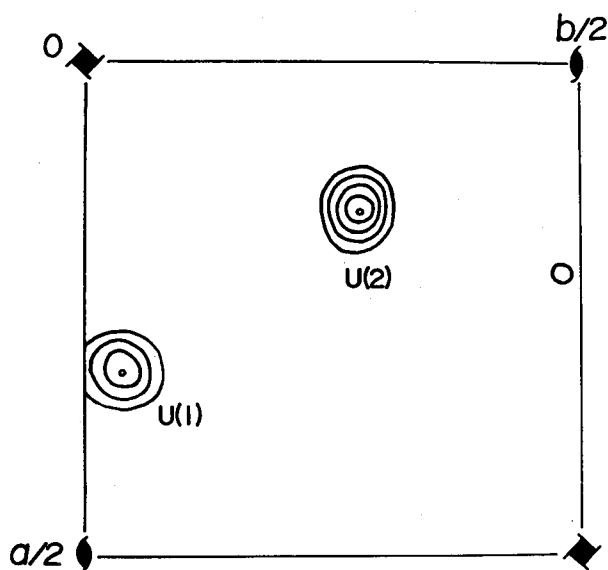


Fig. III-6. Difference Fourier synthesis (uranium-native).
The two peaks due to U1 and U2 are superimposed.

Table III-3. Heavy atom parameters and their estimated standard deviations.

	site 1	site 2
x	0.3105 (4)	0.1486 (3)
y	0.0347 (4)	0.2733 (3)
z	0.5000 ^{a)}	0.6394 (6)
B	30 (4) Å ²	31 (3) Å ²
G ^{b)}	32.0 (6)	41.5 (5)
	$\Delta B = -1.9 (5) \text{ Å}^2$	

a) Parameter fixed during the refinement

b) Effective occupancy in number of electrons

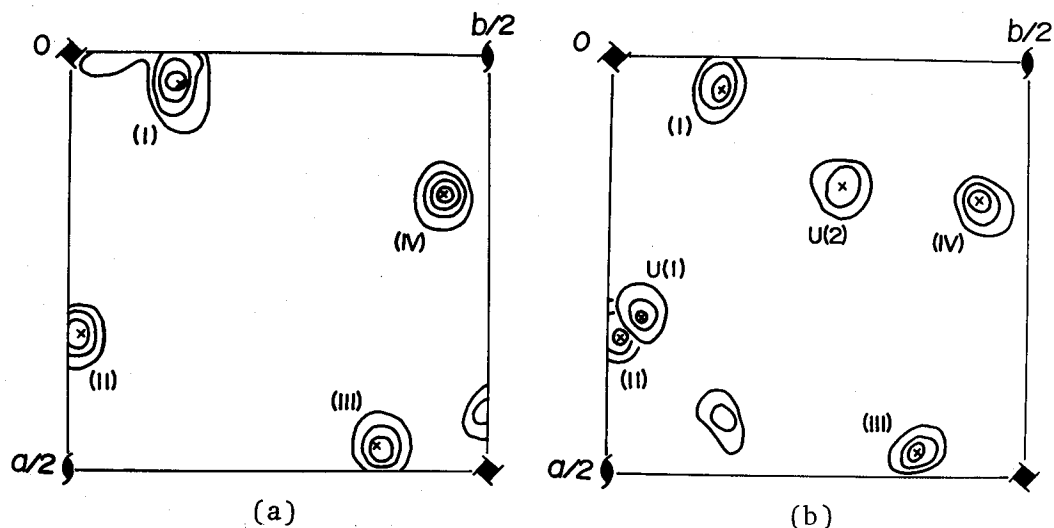


Fig. III-7. Anomalous difference synthesis. The peaks due to the clusters and the heavy atoms are superimposed on one section. The peak without cross mark in each map indicates the maximum background.

Table III-4. The coordinates of the cluster.

Cluster No.	x	y	z	peak height ^{a)}	
				native	derivative
I	0.04	0.13	0.56	100	100
II	0.34	0.01	0.14	86	82
III	0.47	0.37	0.91	88	79
IV	0.17	0.45	0.17	93	88
Other highest ^{b)} peak				60	65

a) The relative height setting the highest peak to be 100.

b) The site of the maximum background in the map for native crystal was different from that for the derivative crystal.

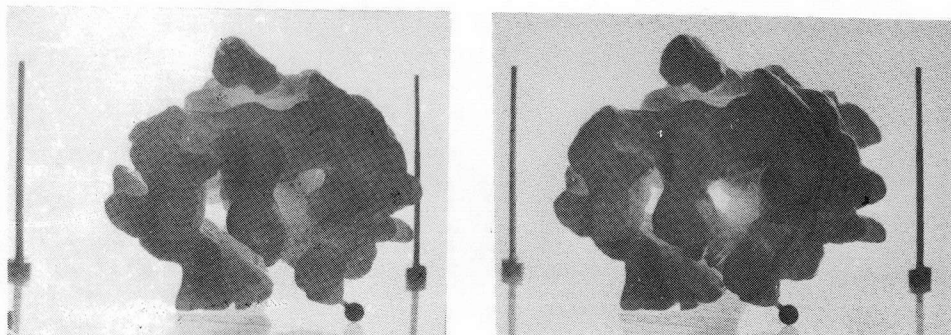


Fig. III-8. Molecular model of *Aphanothece sacrum* ferredoxin at 5 Å resolution. The ball (lower-right) indicates the heavy atom binding site.

IV. Discussion

IV-1. X-Ray analysis

The present crystallographic analysis for chloroplast type ferredoxins was obliged to be proceeded by the single isomorphous replacement method, since only one kind of isomorphous heavy atom derivative was available for the phase determination. The full utilization of the anomalous dispersion effect of the heavy atoms, both heavy atoms introduced by soaking and present in the native crystal, has led to successful structure determination. The improvement of phase angles by the utilization of the anomalous dispersion effect is obvious; the mean figure of merit at 3.5 Å resolution was 0.63 when the anomalous dispersion effect of both native and derivative crystals was utilized, 0.61 when that of the derivative crystal was utilized, and 0.52 when none of this effect was utilized. Although the anomalous dispersion effect has been used recently for the phase determination, the case is rare yet (55) where the protein structure was determined at a resolution of atomic level by the single isomorphous replacement method coupled by the anomalous dispersion effect. The success of this method was based on the accurate intensity measurement of the Bijvoet pair of reflections obtained from the diffractometer equipped with rotating anode X-ray generator. The anomalous dispersion method is free from the problem of lack of isomorphism. Therefore, the more the instrument for the intensity measurement developed, the more the method

is actively applied to solve the phase problem, especially in the case where only one heavy atom derivative is available.

IV-2. Environment of cluster

The cluster is very close to the molecular surface, and the top-rear side of the cluster is exposed to the solvent. Except this side, the cluster is surrounded by polypeptide and hydrophobic side chains. Most of aromatic residues exist in upper-half of the molecule. However, no aromatic ring is contact with the cluster, nor accessible without unfolding of the main chain. It is plausible that these aromatic groups act to make the vicinity of the cluster hydrophobic environment.

The scheme of coordination of cysteinyl sulfur atoms to the cluster has been revealed for the first time for chloroplast type ferredoxin. The schematic representation of the coordination of the cysteine residues is shown in Fig. IV-1, and the structures around the clusters are shown in Fig. IV-2, for both types of ferredoxins. The scheme that two cysteinyl residues, the Cys46 and Cys49, separated by two residues coordinate to different iron atoms is found in chloroplast type ferredoxin as in bacterial ferredoxin (12). Although similarity has been found in peptide conformation that the chain from the sulfur atom of the Cys46 to the nitrogen atom of the Thr48 has 3_{10} turn structure with NH...S hydrogen bond of type I, overall conformation from the Cys46 to Cys49 of chloroplast type ferredoxin is

different from that of bacterial ferredoxin (54). It is difficult to see the similarity of the peptide conformations around the clusters in both types of ferredoxins.

The two iron atoms in chloroplast type ferredoxin are ferric in the oxidized state, and one of them is formally ferrous in the reduced state. It is an intriguing question why the ferredoxin has the redox potential at -0.4 V, which is higher than that of its analog of -1.5 V, although direct comparison is impossible due to different condition of the measurement (34). The difference of the redox potential may be ascribed to the protein structure around the cluster. The existence of the $\text{NH}\cdots\text{S}$ hydrogen bonds may be one of the structural reasons; the negatively charged cluster can be stabilized by the hydrogen bonds. In addition to the three hydrogen bonds between the NH of the main chain and the cysteinyl sulfur atoms as described previously, some $\text{NH}\cdots\text{S}$ hydrogen bonds seem likely to exist between the NH of the main chain and the inorganic sulfur atoms; $\text{NH}(\text{Ala}45)\cdots\text{S}^*$ and $\text{NH}(\text{Cys}49)\cdots\text{S}^*$. The number of the hydrogen bonds per cluster is thus counted as five for chloroplast type ferredoxin, which is comparable with that for bacterial ferredoxin (54). This explanation may be supported by the similar circumstance for bacterial ferredoxin and high-potential iron sulfur protein (HiPIP), both of which have the same $4\text{Fe}-4\text{S}^*$ cluster. The redox potential of its analog is -1.2 V, which is lower than that of the ferredoxin (55). According to the three state hypothesis of Carter *et al.* (56), the cluster in HiPIP in the reduced state is equivalent

to that in bacterial ferredoxin in the oxidized state. If HiPIP is denaturated in 80 % DMSO, the protein is super-reduced at lower potential than that of the ferredoxin (57).

IV-3. Electron transfer mechanism

On the electron transfer mechanism, Carter *et al.* suggested that electron transfer to the cluster was achieved through the aromatic ring of tyrosine residue (58,59). The aromatic ring of Tyr2 is in contact with one 4Fe-4S* cluster and that of Tyr28 with the other cluster in *P. aerogenes* ferredoxin. In addition, similar contact is also found in *Chromatium* HiPIP. Each aromatic ring seems likely to communicate with solvent; the hydroxyl edge of each tyrosyl residue in the ferredoxin is exposed to solvent (12), while that in HiPIP is hydrogen bonded to a water molecule (58). Although some differences are found in the access of the aromatic ring to the cluster in the ferredoxin and HiPIP, the principal interaction of the ring with the cluster occurs via an inorganic sulfur atoms in both cases. The contact of the ring and the cluster is observed also in solution by NMR spectroscopy (60). However, some chemical and spectroscopic evidences are shown against the hypothesis by Lode *et al.* (61). A derivative of *Clostridium acidurici* ferredoxin, in which a leucyl residue has been substituted for one of the tyrosyl residues (in position 2 from the amino terminus), has full activity as an electron carrier in biological assays. If the assumption that electron transfer to or from the cluster is the rate-

limiting step is valid, it is reasonable to conclude that the primary pathway of electron transfer in bacterial ferredoxin is not via the aromatic ring (60).

Although the Tyr39 in the chloroplast type ferredoxin exists near the cluster in the amino acid sequence, the aromatic ring, unlike in bacterial ferredoxin nor in HiPIP, is too far away to interact with the cluster as shown in Fig. IV-3. The approach of the aromatic ring to the cluster is impossible unless the conformation of the main chain changes drastically. In addition, recent amino acid sequence studies have shown that the tyrosine is replaced by other residues as shown in Table I-2 (27). Therefore, it is also unlikely for chloroplast type ferredoxin that the electron transfer occurs via the aromatic ring to the cluster.

Alternative mechanism is possible that electron transfer may occur via the orbitals of the cysteinyl-sulfur atoms, since these residues are directly bonded to the cluster and two of them are exposed to solvent. This mechanism is also possible for bacterial ferredoxin, since the cysteinyl residue bonded to each cluster appears to be exposed to solvent. The denaturation of chloroplast type ferredoxin by mersalyl, which was observed by the fact that the characteristic color of the ferredoxin disappeared by soaking the crystal in the heavy atom solution, suggests that the cysteinyl residues are in place easily accessible to solvent. Similar feature has been reported for spinach ferredoxin (66); the spinach ferredoxin readily reacts with

p-chloromercuribenzoate to disappear its absorption band due to the cluster. Furthermore, the reactivity for the reagent decreased significantly (about 70 times) in the presence of ferredoxin-NADP-reductase under low ionic strength condition. These observations suggest that ferredoxin is bounded by ferredoxin-NADP-reductase to form a complex at the cluster located near the molecular surface, and are consistent with the present electron transfer mechanism. The circumstance mentioned above might make the preparation of the isomorphous heavy atom derivatives difficult resulting that only one kind of the derivative was available.

IV-4. Molecular evolution

The main chain foldings of chloroplast type and bacterial ferredoxins are compared in Fig. IV-4. One of the conspicuous features of the latter is that its three-dimensional structure has two fold symmetry (12). The amino acid sequence study showed subtle correlation between the sequences of both types of ferredoxins (28), and in addition, in the case of cytochrome *c* the three dimensional structures of different species are substantially same in spite of considerable difference in the sequences (62-65), so that the two fold symmetry or trace of the symmetry has been expected in the three dimensional structure of chloroplast type ferredoxin. The conclusion is, however, that there is no trace of the symmetry nor correlation between the two types of ferredoxins.

As the three dimensional structure of chloroplast type ferredoxin is now at hand, it is interesting to examine the amino acid sequences from various species of this type. The invariant residues in the sequences are not randomly distributed, but mainly from residue 36 to 49, from residue 65 to 70, and from residue 75 to 82. The distribution of the differences of amino acid residues is shown in Fig. IV-5. The figure apparently shows that the residues around functionally important cysteinyl residues, Cys41, Cys46, Cys49, and Cys79, are invariant. It may be noteworthy that the segment from 61 to 70 has many invariant residues, and that it locates near the cluster in the three dimensional structure. The invariant residue, Phe65, locates at the left side of the cluster, and appears to prevent solvent from attacking the cluster from this side. The side groups of the residues of the Ser47 and Asp67 appear to hydrogen bonded. The Ser47 and Asp67 are completely invariant in chloroplast type ferredoxins except *P. americana* II ferredoxin (in this ferredoxin Asp at 67 is replaced by Glu, therefore the hydrogen bond with the Ser47 is possible). Therefore, this hydrogen bond may be common for all chloroplast type ferredoxin, and may play an important role to maintain the conformation of the chain at the left side of the cluster. It seems likely from the molecular structure that this segment contacts with ferredoxin-NADP-reductase upon formation of the complex. It has been also reported for bacterial ferredoxin that the invariant residues tend to be concentrated in the vicinity of the clusters (12).

The other feature of the amino acid sequences is that deletions of amino acid residues occur at 10th and 14th in some ferredoxins, where the residue at 11th is invariably proline. The segment around the 10th residue of *S. platensis* ferredoxin, which has the residues at 10th and 14th and no proline at 11th, forms a hair-pin loop. This suggests that the proline residue locates at the corner of the main chain folding to preserve the overall conformation unchanged. While *A. sacrum* ferredoxin lacks the residues at 10th and 14th with the residue at 11th of proline. At 5 Å resolution of *A. sacrum* ferredoxin, however, it can not say more than that the structures of the ferredoxins of *S. platensis* and *A. sacrum* look alike in spite of considerable remoteness in the phylogenetic tree (amino acid residues differ by 30 % in the sequence).

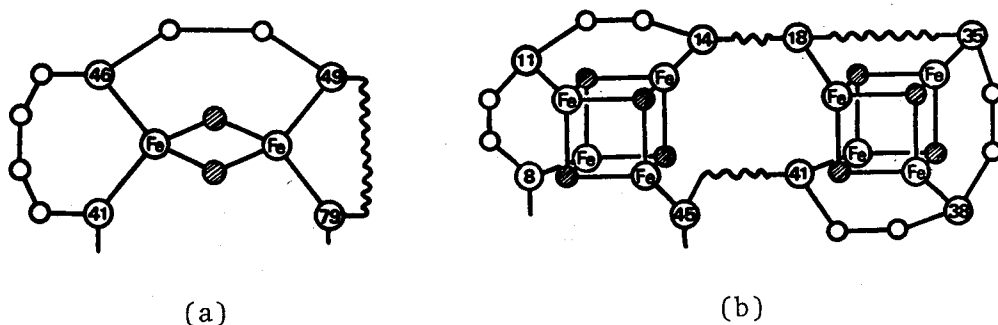


Fig. IV-1. Schematic representation of the coordination of cysteinyl residues to the clusters of (a) chloroplast type and (b) bacterial ferredoxins (12). The shaded circles indicate inorganic sulfur atoms.

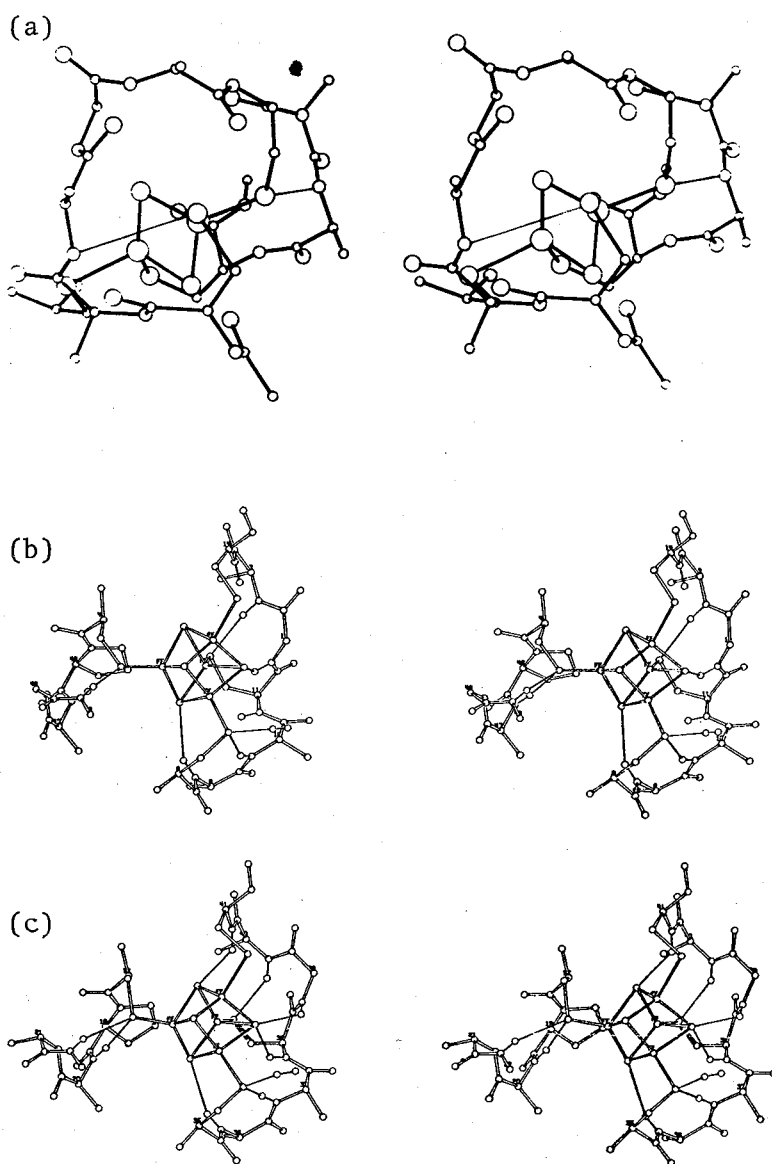


Fig. IV-2. Stereo-drawings of the structures around the clusters. The $\text{NH}\cdots\text{S}$ hydrogen bonds are shown by thin lines. (a) Chloroplast type ferredoxin, (b) and (c) bacterial ferredoxin (12).

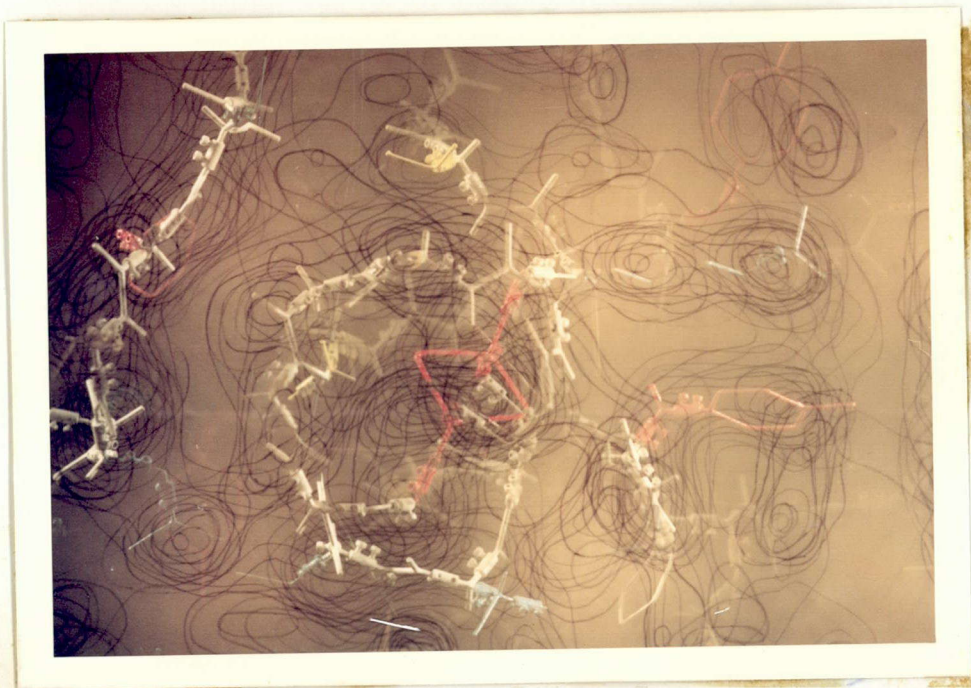
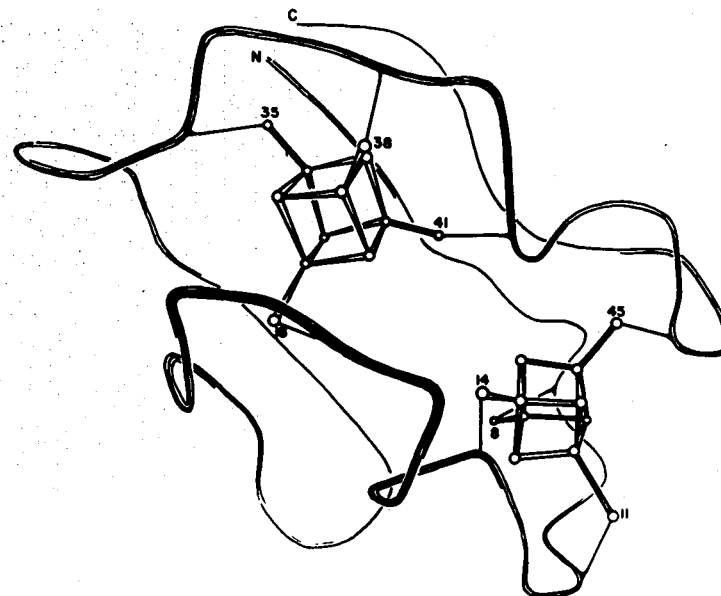


Fig. IV-3. A composite electron density contours with the model. The Tyr39 is directed to solvent. In the left side of the photograph, one can see the segment of Ser64-Phe65-Leu66-Asp67, and the hydrogen bond between the side chains of Ser47 and Asp67 (lower-left). The model shown in the photograph is mirror image.



(a)



(b)

Fig. IV-4. Schematic drawing of the main chain foldings of (a) chloroplast type ferredoxin and (b) bacterial ferredoxin (12). The two fold symmetry disappeared in the structure of chloroplast type ferredoxin.

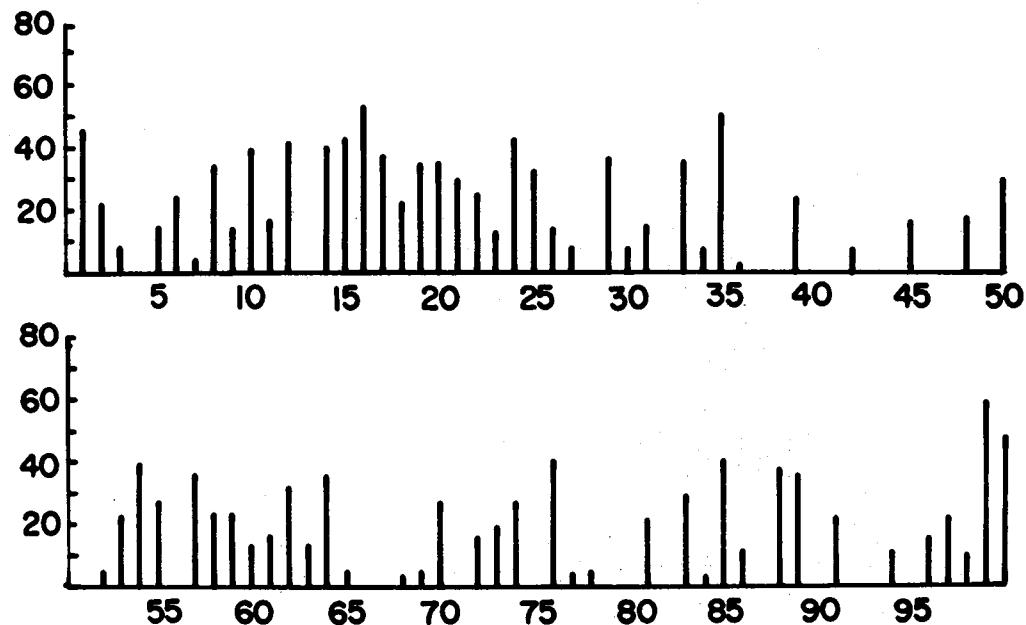


Fig. IV-5. Distribution of the differences of amino acid residues. The horizontal axis is residue number, and vertical axis is the average of the mutation values. The mutation value adopted here is the minimum number of nucleotide changes required to convert the coding from one amino acid to the other (29). The mutation values of 120 pairs of amino acids for each residue number have been calculated on the basis of the sixteen amino acid sequences (Table I-2), and averaged. The mutation value in the figure is multiplied by 100/3.

IV-5. Advance in future

Spirulina platensis and *Aphanothece sacrum* ferredoxins will be further investigated in due course by the accurate intensity measurement of high angle reflections and by application of various kinds of refinements (67,68). The more high resolution analysis may clarify the molecular structure more detail together with the behavior of fixed solvent, and will also resolve the problem how the two chloroplast type ferredoxins are similar.

The structure of chloroplast type ferredoxin is different from that of bacterial ferredoxin, and the correspondence of the molecular structures of both ferredoxins is at present impossible. From the view point of molecular evolution, the ferredoxin of photosynthetic bacterial type may exist in important position; the protein is intermediate in the number of amino acid residues as well as in the number of iron and inorganic sulfur atoms between bacterial and chloroplast type ferredoxins. Therefore, the three dimensional structure of the ferredoxin of this type will give invaluable knowledge on the molecular evolution of ferredoxins.*)

*) The structure analysis of the ferredoxin from *Bacillus thermoproteolyticus* (has no function of photosynthesis) is in progress. The ferredoxin consists of 81 amino acid residues and four iron and four inorganic sulfur atoms. The protein crystallized in triclinic, space group P1, and two molecules are involved in a unit cell. The unit cell

constants are $a=32.96$, $b=37.83$, $c=39.82$ Å, $\alpha=118.10$, $\beta=104.17$, $\gamma=89.69^\circ$. The precession photograph is shown in Fig. IV-6, and showed that the X-ray diffractions are measurable to more than 1.8 Å resolution. The intensity data of the Bijvoet pairs were collected with Ni-filtered $\text{CuK}\alpha$ radiation. This protein crystal showed marked stability against the X-ray compared with *S. platensis* or *A. sacrum* ferredoxin: the decay of the crystal was only a few percents during the intensity measurement of 10,000 reflections. Therefore, the intensities were corrected only for the Lorentz and polarization and absorption effects. Difference Patterson function (Fig. IV-7), based on the anomalous differences of the native crystal at 5 Å resolution, showed one large peak due to the cluster-cluster vector.

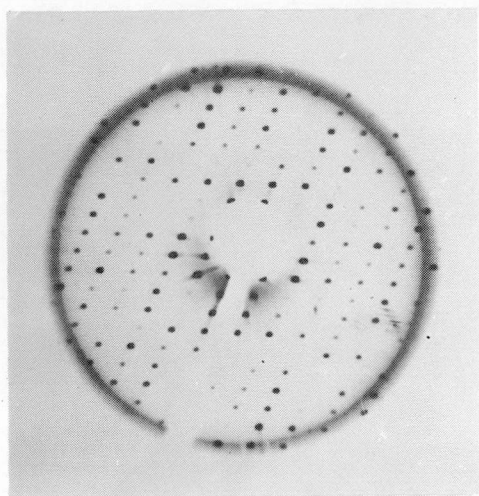


Fig. IV-6. Precession photograph of *B. thermoproteolyticus* ferredoxin.

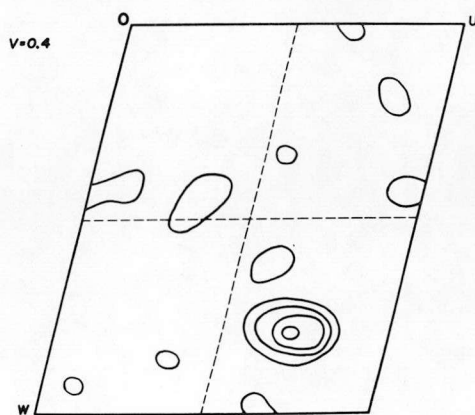


Fig. IV-7. Difference Patterson function at 5 Å resolution.

References

- 1) L. E. Mortenson, R. C. Valentine, and J. E. Carnahan, *Biochem. Biophys. Res. Commun.*, 7, 448 (1962).
- 2) R. C. Valentine, R. L. Jackman, and R. S. Wolfe, *Biochem. Biophys. Res. Commun.*, 7, 453 (1962).
- 3) B. B. Buchanan, W. Lovenberg, and J. C. Rabinowitz, *Proc. Nat. Acad. Sci. USA*, 49, 345 (1963).
- 4) K. Tagawa and D. I. Arnon, *Nature*, 195, 537 (1962).
- 5) D. I. Arnon, *Science*, 149, 1460 (1965).
- 6) H. E. Davenport, R. Hill, and F. R. Whatley, *Proc. Roy. Soc. London, Ser. B*, 139, 346 (1952).
- 7) D. I. Arnon, F. R. Whatley, and M. B. Allen, *Nature*, 180, 182, 1325 (1957).
- 8) A. San Pietro and H. M. Lang, *J. Biol. Chem.*, 231, 211 (1958).
- 9) H. E. Davenport and R. Hill, *Biochem. J.*, 74, 493 (1960).
- 10) "Iron-Sulfur Proteins", Vol. I, II (ed. W. Lovenberg), Academic Press, New York (1973).
- 11) M. Tanaka, T. Nakashima, A. Benson, H. F. Mower, and K. T. Yasunobu, *Biochem. Biophys. Res. Commun.*, 16, 422 (1964).
- 12) E. T. Adman, L. C. Sieker, and L. H. Jensen, *J. Biol. Chem.*, 248, 3987 (1973).
- 13) D. O. Hall, R. Cammack, and K. K. Rao, *Pure and Applied Chem.*, 34, 553 (1973).
- 14) D. H. Petering and G. Palmer, *Arch. Biochem. Biophys.*, 141, 456 (1970).

- 15) J. F. Gibson, D. O. Hall, J. H. M. Thonley, F. R. Whatley, *Proc. Nat. Acad. Sci. USA*, 56, 987 (1966).
- 16) G. Palmer, W. R. Dunham, J. A. Fee, R. H. Sands, T. Iizuka, and T. Yonetani, *Biochem. Biophys. Acta*, 245, 201 (1971).
- 17) W. R. Dunham, A. J. Bearden, I. T. Salmeen, G. Palmer, R. H. Sands, W. H. Orme-Johnson, and H. Beinert, *Biochem. Biophys. Acta*, 253, 134 (1971).
- 18) K. Tagawa and D. I. Arnon, *Biochem. Biophys. Acta*, 153, 602 (1968).
- 19) G. Palmer and R. H. Sands, *J. Biol. Chem.*, 241, 253 (1966).
- 20) D. I. Arnon, H. Y. Tsujimoto, and B. D. McSwain, *Nature*, 214, 562 (1967).
- 21) M. Shin, K. Tagawa, and D. I. Arnon, *Biochem. Z.*, 338, 84 (1963).
- 22) J. R. Mortenson, R. C. Valentine, and J. E. Carnahan, *J. Biol. Chem.*, 238, 794 (1963).
- 23) J. R. Postgate, *Nature*, 226, 25 (1970).
- 24) R. H. Hageman and D. P. Hucklesby, *Methods in Enzymol.*, 23, (part A) 491 (1971).
- 25) R. Bachofen, B. B. Buchanan, and D. I. Arnon, *Proc. Nat. Acad. Sci. USA*, 51, 690 (1964).
- 26) P. J. Lea and B. J. Milflin, *Biochem. Biophys. Res. Commun.*, 64, 856 (1975).
- 27) S. Wakabayashi, T. Hase, K. Wada, H. Matsubara, K. Suzuki, and S. Takaichi, *J. Biochem.*, 83, 1305 (1978).

- 28) H. Matsubara and R. M. Sasaki, *J. Biol. Chem.*, 243, 1732 (1968).
- 29) W. M. Fitch and E. Margoliash, *Science*, 155, 279 (1967).
- 30) H. Matsubara, R. M. Sasaki, D. K. Tsuchiya, and M. C. W. Evans, *J. Biol. Chem.*, 245, 2121 (1970).
- 31) R. Bachofen and D. I. Arnon, *Biochem. Biophys. Acta*, 120, 259 (1966).
- 32) S. Kereztes-Nagy and E. Margoliash, *J. Biol. Chem.*, 241, 5955 (1966).
- 33) W. R. Dunham, G. Palmer, R. H. Sands, and A. J. Bearden, *Biochem. Biophys. Acta*, 253, 373 (1971).
- 34) J. J. Mayerle, R. B. Frankel, R. H. Holm, J. A. Ibers, W. D. Phillips, and J. F. Weiher, *Proc. Nat. Acad. Sci. USA*, 70, 2429 (1973).
- 35) K. Wada, T. Hase, H. Tokunaga, and H. Matsubara, *FEBS Letters*, 55, 102 (1975).
- 36) K. Wada, H. Kagamiyama, M. Shin, and H. Matsubara, *J. Biochem.*, 76, 1217 (1974).
- 37) B. W. Matthews, *J. Mol. Biol.*, 33, 491 (1968).
- 38) T. L. Blundel and L. N. Johnson, "Protein Crystallography", Academic Press, London (1976).
- 39) A. C. T. North, D. C. Phillips, and F. S. Matthews, *Acta Crystallogr.*, A24, 351 (1968).
- 40) A. J. C. Wilson, *Acta Crystallogr.*, 2, 318 (1949).
- 41) D. M. Blow, *Proc. Roy. Soc.*, A247, 302 (1958).
- 42) M. G. Rossmann, *Acta Crystallogr.*, 13, 221 (1960).
- 43) A. K. Singh and S. Ramaseshan, *Acta Crystallogr.*, 21, 279 (1966).

- 44) R. E. Dickerson, J. C. Kendrew, and B. E. Strandberg, *Acta Crystallogr.*, 14, 1188 (1961).
- 45) R. E. Dickerson, M. L. Kopka, J. C. Varnum, and J. E. Weinzierl, *Acta Crystallogr.*, 23, 511 (1967).
- 46) D. M. Blow and M. G. Rossmann, *Acta Crystallogr.*, 14, 1195 (1961).
- 47) B. W. Matthews, *Acta Crystallogr.*, 20, 82 (1966).
- 48) G. Strahs and J. Kraut, *J. Mol. Biol.*, 35, 503 (1968).
- 49) W. A. Hendrickson and E. E. Latteman, *Acta Crystallogr.*, B26, 136 (1970).
- 50) F. M. Richards, *J. Mol. Biol.*, 37, 225 (1968).
- 51) R. E. Marsh and J. Donohue, *J. Adv. Prot. Chem.*, 22, 235 (1967).
- 52) W. D. S. Motherwell, PLUTO (1967), a program for plotting molecular and crystal structures, Cambridge Crystallographic file user manual.
- 53) J. Donohue, *J. Mol. Biol.*, 45, 231 (1969).
- 54) E. Adman, K. D. Watenpaugh, and L. H. Jensen, *Proc. Nat. Acad. Sci. USA*, 72, 4854 (1975).
- 55) T. Herskovitz, B. A. Averill, R. H. Holm, J. A. Ibers, W. D. Phillips, and J. F. Weiher, *Proc. Nat. Acad. Sci. USA*, 69, 2437 (1972).
- 56) C. W. Carter, J. Kraut, S. T. Freer, R. A. Alden, L. C. Sieker, E. Adman, and L. H. Jensen, *Proc. Nat. Acad. Sci. USA*, 69, 3526 (1972).
- 57) R. Cammack, *Biochem. Biophys. Res. Commun.*, 54, 548 (1973).
- 58) C. W. Carter, J. Kraut, S. T. Freer, and R. A. Alden, *J. Biol. Chem.*, 249, 6339 (1974).

- 59) C. W. Carter, J. Kraut, S. T. Freer, N. Xuong, R. A. Alden, and R. G. Bartsch, *J. Biol. Chem.*, 249, 4212 (1974).
- 60) E. L. Packer, H. Sternlicht, and J. C. Rabinowitz, *Proc. Nat. Acad. Sci. USA*, 69, 3278 (1972).
- 61) E. T. Lode, C. L. Murray, W. V. Sweeney, and J. C. Rabinowitz, *Proc. Nat. Acad. Sci. USA*, 71, 1361 (1974).
- 62) R. E. Dickerson, T. Takano, D. Eisenberg, O. B. Kallai, L. Samson, A. Cooper, and E. Margoliash, *J. Biol. Chem.*, 246, 1511 (1971).
- 63) T. Takano, O. B. Kallai, R. Swanson, and R. E. Dickerson, *J. Biol. Chem.*, 248, 5234 (1973).
- 64) F. R. Salemme, S. T. Freer, N. H. Xuong, R. A. Alden, and J. Kraut, *J. Biol. Chem.*, 248, 3910 (1973).
- 65) N. Tanaka, T. Yamane, T. Tsukihara, T. Ashida, and M. Kakudo, *J. Biochem.*, 77, 147 (1975).
- 66) H. Hasumi and S. Nakamura, *J. Biochem.*, 84, 707 (1978).
- 67) R. Diamond, *Acta Crystallogr.*, 21, 253 (1966).
- 68) R. Diamond, *Acta Crystallogr.*, A27, 436 (1971).

List of publications

- 1) Topochemical Studies. I. The Crystal and Molecular Structure of Potassium Dihydrogen *trans*-Aconitate, $K^+(HOOC.CH_2.C(COOH)=COO)$.
K. Fukuyama, S. Kashino, and M. Haisa, *Chem. Lett.* 1972, 599-602.
- 2) The Crystal and Molecular Structure of *p*-Hydroxybenzoic Acid Monohydrate.
K. Fukuyama, K. Ohkura, S. Kashino, and M. Haisa, *Bull. Chem. Soc. Japan*, 46, 804-808 (1973).
- 3) The Crystal Structure of Piperidinium *p*-Hydroxybenzoate.
K. Fukuyama, S. Kashino, and M. Haisa, *Acta Cryst.*, B29, 2713-2717 (1973).
- 4) The Crystal Structure of (+)-1-Benzyl-5-phenyl-1-azacycloheptan-4-one Hydrochloride, $C_{19}H_{21}NO.HCl$.
K. Fukuyama, S. Shimizu, S. Kashino, and M. Haisa, *Bull. Chem. Soc. Japan*, 47, 1117-1121 (1974).
- 5) The Crystal and Molecular Structure of Sterigmatin, A Metabolite of *Aspergillus versicolor*.
K. Fukuyama, T. Tsukihara, Y. Katsube, T. Hamasaki, Y. Hatsuda, N. Tanaka, T. Ashida, and M. Kakudo, *Bull. Chem. Soc. Japan*, 48, 1639-1640 (1975).
- 6) The Crystal and Molecular Structure of the *p*-Bromobenzoate of Sterigmatocystin.
K. Fukuyama, T. Tsukihara, Y. Katsube, N. Tanaka, T. Hamasaki, and Y. Hatsuda, *Bull. Chem. Soc. Japan*, 48, 1980-1983 (1975).

- 7) The Crystal and Molecular Structure of Versicolorin C,
A Metabolite of *Aspergillus versicolor*.
K. Fukuyama, T. Tsukihara, Y. Katsube, T. Hamasaki,
and Y. Hatsuda, *Bull. Chem. Soc. Japan*, 48, 2648-
2652 (1975).
- 8) The Crystal and Molecular Structure of Emericellin,
A Metabolite of *Aspergillus nidulans*.
K. Fukuyama, T. Tsukihara, S. Kishida, Y. Katsube,
M. Ishida, T. Hamasaki, and Y. Hatsuda, *Bull. Chem.
Soc. Japan*, 48, 2947-2948 (1975).
- 9) A Structure Analysis of a Bromo Derivative of Parasiti
colide A by the X-Ray Diffraction Method.
K. Fukuyama, H. Kawai, T. Tsukihara, K. Tsukihara,
Y. Katsube, T. Hamasaki, Y. Hatsuda, and H. Kuwano,
Bull. Chem. Soc. Japan, 48, 2949-2950 (1975).
- 10) A Structure Analysis of Bromoacetate of Hydroxypipere-
none by the X-Ray Diffraction Method.
K. Matsui, K. Fukuyama, K. Tsukihara, T. Tsukihara,
Y. Katsube, and K. Munakata, *Bull. Chem. Soc. Japan*,
49, 62-65 (1976).
- 11) The Crystal Structures of Sterigmatocystin and O-Methyl-
sterigmatocystin, Metabolites of the Genus *Aspergillus*.
K. Fukuyama, K. Hamada, T. Tsukihara, Y. Katsube,
T. Hamasaki, and Y. Hatsuda, *Bull. Chem. Soc. Japan*,
49, 1153-1154 (1976).
- 12) Structural Analysis of Sydowic Acid by X-ray Diffraction.
K. Fukuyama, T. Tsukihara, Y. Katsube, T. Hamasaki,

- and Y. Hatsuda, *Agr. Biol. Chem.*, 40, 1053-1054 (1976).
- 13) Structure of Versiol, A New Metabolite from *Aspergillus versicolor*.
K. Fukuyama, T. Tsukihara, Y. Katsube, T. Hamasaki,
and Y. Hatsuda, *Tetrahedron Letters*, 1976, 189-190.
- 14) A Structure Analysis of Pieristoxin G by the X-Ray
Diffraction Method.
K. Fukuyama, T. Tsukihara, Y. Katsube, M. Katai, and
H. Meguri, *Chem. Pharm. Bull.*, 24, 2775-2780 (1976).
- 15) 5,6-Dimethoxysterigmatocystin, A New Metabolite from
Aspergillus multicolor.
T. Hamasaki, T. Nakagomi, Y. Hatsuda, K. Fukuyama,
and Y. Katsube, *Tetrahedron Letters*, 1977, 2765-2766.
- 16) Determination of Absolute Configuration of Epishami-
xanthone, a Metabolite of *Aspergillus rugulosus*, by
Anomalous Scattering of Light Atoms.
K. Fukuyama, K. Hamada, T. Tsukihara, and Y. Katsube,
Bull. Chem. Soc. Japan, 51, 37-44 (1978).
- 17) Structure and Absolute Configuration of Versiol, a
Metabolite from *Aspergillus versicolor*.
K. Fukuyama, Y. Katsube, T. Hamasaki, and Y. Hatsuda,
J. Chem. Soc. Perkin Trans. II, 1978, 683-686.
- 18) Absolute Configurations of Asperlin, a Metabolite of
Aspergillus nidulans, and Its Related Compounds.
K. Fukuyama, Y. Katsube, A. Noda, T. Hamasaki, and
Y. Hatsuda, *Bull. Chem. Soc. Japan*, 51, 3175-3181
(1978).

- 19) Crystallization and a 5 Å X-ray Diffraction Study of *Aphanothece sacrum* Ferredoxin.
- A. Kunita, M. Koshibe, Y. Nishikawa, K. Fukuyama, T. Tsukihara, Y. Katsube, Y. Matsuura, N. Tanaka, M. Kakudo, T. Hase, and H. Matsubara, *J. Biochem.*, 84, 989-992 (1978).
- 20) X-Ray Analysis of Ferredoxin from *Spirulina platensis*.
- II. Chelate Structure of Active Center.
- T. Tsukihara, K. Fukuyama, H. Tahara, Y. Katsube, Y. Matsuura, N. Tanaka, M. Kakudo, K. Wada, and H. Matsubara, *J. Biochem.*, 84, 1645-1647 (1978).
- 21) The Crystal and Molecular Structures of 6-Deoxyversicolorin A and Versicolorin A, Metabolites from *Aspergillus versicolor*.
- K. Fukuyama, T. Ashida, Y. Katsube, and M. Kakudo, *Bull. Chem. Soc. Japan*, 52, 677-683 (1979).